Design, kinematics, and control of a soft spatial fluidic elastomer manipulator

Andrew D. Marchese and Daniela Rus

Abstract

This paper presents a robotic manipulation system capable of autonomously positioning a multi-segment soft fluidic elastomer robot in three dimensions. Specifically, we present an extremely soft robotic manipulator morphology that is composed entirely from low durometer elastomer, powered by pressurized air, and designed to be both modular and durable. To understand the deformation of a single arm segment, we develop and experimentally validate a static deformation model. Then, to kinematically model the multi-segment manipulator, we use a piece-wise constant curvature assumption consistent with more traditional continuum manipulators. In addition, we define a complete fabrication process for this new manipulator and use this process to make multiple functional prototypes. In order to power the robot's spatial actuation, a high capacity fluidic drive cylinder array is implemented, providing continuously variable, closed-circuit gas delivery. Next, using real-time data from a vision system, we develop a processing and control algorithm that generates realizable kinematic curvature trajectories and controls the manipulator's configuration along these trajectories. Lastly, we experimentally demonstrate new capabilities offered by this soft fluidic elastomer manipulation system such as entering and advancing through confined three-dimensional environments as well as conforming to goal shape-configurations within a sagittal plane under closed-loop control.

Keywords

Flexible arms, mechanics, design and control, biologically-inspired robots, human-centered and life-like robotics, dexterous manipulation, manipulation

1. Introduction

Manipulators with rigid links and discrete joints provide optimal solutions for automation, where fast, precise, and controllable motions are utilized for repetitive tasks in structured and often static environments; however, in natural environments and in human-centric operations, where safety and adaptability to uncertainty are fundamental requirements, soft robots may serve as a better alternative. By studying a completely *soft* and *compliant* robot, we can begin to identify appropriate hardware processes, kinematic models, and control strategies for a growing class of robots designed to incorporate *softness*.

In this work we present a completely soft spatial manipulation system (see Figure 1). That is, we provide the design, fabrication, and kinematic modeling of a new manipulator morphology: a fluid-powered three-dimensional multi-segment arm composed entirely of soft elastomer. In addition, we develop a power system as well as processing and control algorithms that enable autonomous closed-loop control of the soft manipulator. We show how the fluidic elastomer manipulator's continuum kinematics

and soft material composition lead to several distinct advantages when compared to traditional rigid body manipulators. First, we show that the manipulator's soft segments deform according to constant curvature. With a constant curvature assumption (Webster and Jones, 2010), we can parameterize this *N*-link spatial soft manipulator with $2N$ joint variables. Second, the kinematics and extreme compliance of such a soft manipulator enable it to fit within and advance through confined environments. When the boundaries of the environment can be parameterized by curved cylinders and its curvature is non-zero, an idealized soft fluidic elastomer manipulator will be more capable of advancing through a confined environment than a

Computer Science and Artificial Intelligence Laboratory, Massachusetts Institute of Technology, USA

Corresponding author:
Andrew D. Marchese, Computer Science and Artificial Intelligence Laboratory, Massachusetts Institute of Technology, 32 Vassar Street, Cambridge, MA 02139, USA.
Email: andy@csail.mit.edu

Fig. 1. Soft fluidic elastomer manipulator gently taking a small ball from the palm of its human collaborator. The manipulator's entirely soft composition and kinematic controller allow it to safely interact with its environment. Reproduced with kind permission from Mary Ann Liebert Inc. (Marchese et al., 2015a).

manipulator with rigid links and discrete joints. We demonstrate this concept experimentally. Third, the continuum kinematics of a soft fluidic elastomer manipulator enable a high degree of dexterity. Specifically, in an environment where a collision-free path is parameterized by a curved path, the continuum kinematics of a fluidic elastomer manipulator can generally fit the curvature of the path better than a rigid link manipulator with discrete joints and rigid links.

Such new capabilities require innovation in both hardware and modeling. The concept of using very soft elastic materials to construct autonomous robots is relatively new and radically different from the time-tested design and fabrication methodologies of traditional robotic systems. As soft roboticists, we are in the process of defining long-lasting morphologies for soft machines. Accordingly, a considerable amount of innovation is required to design functional soft machines, to develop processes by which these machines can be repeatably fabricated, and to engineer systems that drive their actuation.

1.1. A Review of soft manipulator designs

Soft machines have many distinguishing design characteristics when compared to traditional hard robots. These differences are reviewed by Trivedi et al. (2008). Soft robots have continuously deformable backbones providing theoretically infinite degrees of freedom (DOFs). This attribute classifies soft robots as a subclass of continuum robots, as reviewed by Robinson and Davies (1999); however, not all continuum robots are truly *soft*, and even continuum robots referred to as *soft* have varying degrees of rigidity.

1.1.1. Discrete hyper-redundant manipulators. Before reviewing the spectrum of continuum manipulator designs,

it is important to mention the discrete hyper-redundant robot configuration. In contrast to continuum robots, this configuration generally has a kinematically constraining backbone composed of multiple rigid links serially connected by revolute joints. Thus, this backbone has many actuatable DOFs and approximates continuous body bending. Examples of discrete hyper-redundant robot manipulators include the 32 DOFs elephant trunk manipulator developed in Hannan and Walker (2003) and the 10 DOFs snake arm robot developed in Buckingham (2002). Another discrete hyper-redundant morphology is the variable geometry truss manipulator (VGTM) as initially explored in Miura et al. (1985) and Miura and Furuya (1988). These designs also use discrete body links; however, here a link is composed of two parallel prismatic joints held at the top and bottom by rigid plates. Each of these body elements resembles a parallel manipulator. A notable variable geometry truss manipulator is the planar prototype developed by Chirikjian and Burdick (1994) with 10 body modules and 30 DOFs.

1.1.2. Hard continuum manipulators. As mentioned, continuum manipulators are realized through a spectrum of morphologies. Many continuum manipulators are composed of hard, but flexible material (e.g. materials having a Young's modulus of roughly 0.5 to 200 GPa). For example, the elastic elephant trunk manipulator developed in Cieslak and Morecki (1999) is composed of eight elastic elements having coil spring backbones and is controlled as three independent body segments yielding six DOFs. In addition, Gravagne et al. (2003) and Gravagne and Walker (2002) model and control the Clemson Tentacle Manipulator, a hard continuum manipulator. This platform has two planar sections, a total of four DOFs, and uses a spring steel backbone. Air-Octor developed in McMahan et al. (2005), the articulated catheter robot developed in Camarillo et al. (2009), and Tubot developed in Sanan et al. (2011) are also examples of continuum manipulators constructed of hard, but flexible materials. The aforementioned hard continuum manipulators use tendons to control bending. Typically, an array of servomotors or linear actuators are used to pull cables that move connecting plates located between body segments.

1.1.3. Semi-soft continuum manipulators. There are softer continuum manipulator morphologies that use a combination of soft and hard components. In these designs, distributed pneumatic muscle actuators (PMAs) are most prevalent, as the review by Trivedi et al. (2008) explains. OctArm IV developed by McMahan et al. (2006) is a notable example. This robot uses 18 PMAs distributed throughout four arm segments yielding 12 DOFs. It is capable of adaptively manipulating and grasping unknown objects that vary in both size and shape (McMahan et al., 2006). Another example is the continuum manipulator developed by Pritts and Rahn (2004) that uses 14 PMAs within two body

segments yielding six DOFs. Also, the continuum manipulator developed by Kang et al. (2013) uses 24 PMAs within six body segments yielding 18 DOFs. Common features among all these designs are rigid end plates to which the PMAs are mounted and actuation pressures of between 50 and 100 psi. Accordingly, this manipulator morphology still relies on rigid components and undergoes significant strain stiffening, a phenomenon that adds rigidity to these robots.

1.1.4. Soft continuum robots. Constructing the body of a continuum robot from soft elastic material likely began with Suzumori et al. (1991) who developed pneumatically actuated rubber segments capable of bidirectional bending. These Flexible Microactuators (FMAs) were fiber-reinforced and explored in the context of both a manipulator and multi-fingered hand. More recently, soft roboticists have made many notable low durometer rubber robots. For example, several rolling belts have been produced by Correll et al. (2010); Onal et al. (2011) and Marchese et al. (2011). Onal and Rus (2013) emulated the serpentine locomotion of snakes, Trimmer et al. (2006) and Umedachi et al. (2013) emulated the peristaltic locomotion of caterpillars, and Marchese et al. (2014c) and Katzschmann et al. (2014) emulated the flapping propulsion of fish. Shepherd et al. (2011) and Tolley et al. (2014) developed walking robots, and Shepherd et al. (2013) developed a jumping robot.

1.1.5. Soft continuum manipulators. Recently, continuum manipulators composed from soft elastic material have been developed. These soft rubber manipulators can be categorized under two primary morphologies. First, there are tendon driven arms consisting of variable length tendons, typically cables or shape memory alloy wire, embedded within and anchored to portions of a soft silicone arm. For example, previous work on soft bio-inspired octopus-like arms developed by Calisti et al. (2010) used tendons and demonstrate capabilities like grasping (Laschi et al., 2012) and locomotion (Calisti et al., 2011). Also, Wang et al. (2013) developed a cable driven soft rubber arm consisting of one large actuated segment that bends bi-directionally. Lastly, McEvoy and Correll (2014) used a programmable stiffness spine in conjunction with tendons to achieve shape change in a soft rubber arm. The second morphology uses fluidic elastomer actuators distributed among the manipulator's soft body segments. In short, this consists of embedding independently actuatable agonistic fluidic channels within each of the arm's soft elastic body segments. When fluid within these channels is pressurized, stress is induced in the elastic body producing localized strain. This strain in combination with a relatively inextensible backbone produces body segment bending. The primary advantages of using fluidic actuation for soft continuum manipulators is that this energy transmission system:

- can be lightweight making for easy integration into distal locations of the body;

- conforms to the time varying shape of the manipulator; and
- does not require rigid components to implement.

Deimel and Brock (2013) developed a pneumatically actuated three-fingered hand made of reinforced silicone that is mounted to a hard industrial robot and capable of robust grasping. More recently, they have developed an anthropomorphic soft pneumatic hand capable of dexterous grasps (Deimel and Brock, 2014). In addition, we have previously shown planar manipulation is possible with an entirely soft robot. That is, a six-segment planar fluidic elastomer robot can be precisely positioned using a closed-loop kinematic controller (Katzschmann et al., 2015; Marchese et al., 2014a,b). Another relevant piece of work is the manually operated three-dimensional elastomer tentacles developed by Martinez et al. (2013) containing nine pneumatic crescent-shaped channels (PneuNets) embedded within three body segments.

1.1.6. Design contributions. However, the manipulator presented in this work differs from these prior works in several important ways:

1. This arm is composed of 100% soft silicone rubber. The arm is modular in both design and fabrication and each module or arm segment has four fluidic actuators and moves in three spatial dimensions.
2. The manipulator has features such as a hollow cylindrical interior and soft segment endplates. The hollow interior accommodates fluid transmission lines and allows modular assembly. Markers placed on segment endplates allow an external vision system to capture the segment endpoint positions. Both of these features are essential to an autonomous manipulation system.
3. The arm has a longitudinally tapering clover-shaped exterior and this morphology has a significant impact on the manipulator's dynamics (Marchese et al., 2015b).

1.2. A Review of soft manipulator kinematics

1.2.1. Robot-independent model. Despite the variability in continuum manipulator designs, their kinematics can often be represented using a piece-wise constant curvature (PCC) model. This is the message within a 2010 review of continuum robots by Webster and Jones (2010). That is, Webster and Jones review several seemingly distinct kinematic modeling approaches, but show that when using a PCC modeling assumption, these approaches yield identical robot-independent results. This assumption means each body segment of a multi-segment arm is assumed to deform with constant curvature. An early use of PCC modeling appears in Hannan and Walker (2003) where a bending robotic trunk is developed.
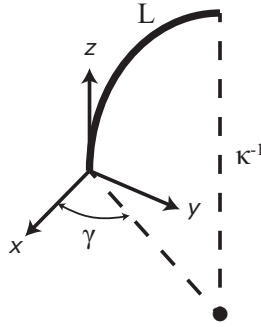
Fig. 2. Arc parameters arc length **L**, curvature **κ**, and plane orientation **γ** used to model the bending of a spatial continuum segment under the PCC assumption. This figure is adapted from Webster and Jones (2010).

Again as Webster and Jones (2010) describe, the transformation from configuration space consisting of arc length **L**, curvature **κ**, and plane orientation **γ** (see Figure 2) to task space consisting of Cartesian position and orientation or pose can be derived in multiple ways. Differential geometry (Hannan and Walker, 2003) or the use of virtual links and a Denavit–Hartenberg approach (Jones and Walker, 2006a) are among a few of the derivations. The robot-independent forward kinematic transformation for a single continuum segment is

$$\mathbf{T} = \begin{bmatrix} \cos\gamma\cos\kappa s & -\sin\gamma & \cos\gamma\sin\kappa s & \frac{\cos\gamma(1-\cos\kappa s)}{\kappa} \\ \sin\gamma\cos\kappa s & \cos\gamma & \sin\gamma\sin\kappa s & \frac{\sin\gamma(1-\cos\kappa s)}{\kappa} \\ -\sin\kappa s & 0 & \cos\kappa s & \frac{\sin\kappa s}{\kappa} \\ 0 & 0 & 0 & 1 \end{bmatrix}$$

where $s = [0, L]$. Although the PCC modeling assumption is quite powerful, it does not always apply to continuum manipulators. The obvious limitation being that not *all* continuum robots deform according to segmented constant curvature. A common exception is when a continuum body segment assumes a spiral, i.e. curvature increases from the segment's base to tip. Mahl et al. (2013) develop general variable curvature continuum kinematics for this reason. Giorelli et al. (2012) develop forward and Jacobian based inverse kinematics for a planar conical soft manipulator that again spirals. Accordingly, an important contribution of this work is that we validate this PCC modeling assumption in the context of a soft fluid-powered elastomer manipulator.

1.2.2. Robot-dependent model. A robot specific mapping is required from actuation space (e.g. tendon lengths or pressures) to configuration space (i.e. **L**, **κ**, and **γ**) as reviewed in Webster and Jones (2010). Previous work on continuum robots has generally approached this robot dependent mapping or model in three ways.

First, Gravagne et al. (2003), Webster et al. (2009) and Trivedi et al. (2008) use Bernoulli–Euler beam mechanics to predict the deformation of continuum robots. When a beam is subject to a tip moment, the beam moment M_b

along the length l is constant, $M_b(l) = c$, and it deforms under constant curvature, $\kappa = M_b/(EI)$. A common realization of this is an actuator parallel to the beam's neutral axis that applies a load to a fixture mounted orthogonal to the beam at the tip. This modeling approach does not apply to our device as it has a fundamentally different operating principle: the soft segment stores bending energy in its outermost actuated layer as opposed to its inner backbone. If the inner layer is assumed to store bending energy, and the Bernoulli–Euler beam model is applied, a non-constant moment along the backbone is predicted producing non-constant deformation.

Second, continuum robots with high pressure (50–100 psi max) (McMahan et al., 2006; Kang et al., 2013; Suzumori et al., 1991) and medium pressure (30 psi max) (Chen et al., 2006) PMAs as well as tendons and cables (Jones and Walker, 2006b; Hannan and Walker, 2003; McMahan et al., 2005; Wang et al., 2013) first make the assumption that segments are deforming under constant curvature and second make the assumption that actuators either lengthen or shorten as a function of input. Subsequently, a relationship between joint variables, i.e. three or four actuator lengths, and constant curvature arc parameters are developed. This approach does not generally apply to our device as the low durometer rubber composition and lack of kinematic constraints means our actuators are expanding spatially at varying rates, not only expanding axially.

Lastly, and perhaps most relevant are robot specific models developed to understand the deformation of extremely soft low pressure fluidic actuators. Onal et al. (2011) develop a static analytical model under the conditions of:

- only longitudinal strain;
- uniform rectangular channels with square cross-sections orthogonal to the bending axis
- a rectangular actuator shape; and
- and stresses that are based on initial channel geometry.

Marchese et al. (2014c) extend this approach to analytical modeling and account for unequal radial and longitudinal strain as well as non-uniform square channels orthogonal to the bending axis. Shepherd et al. (2011) develop a model that assumes equal longitudinal and radial strain in uniform round channels orthogonal to the bending axis in a rectangular actuator and use a linear stress-strain relationship. These models all assume a two-dimensional cross-section of infinite thickness.

1.2.3. Modeling contributions. An important contribution of this work is that we show the viability of the PCC modeling assumption in the context of a spatial fluidic elastomer manipulator. We also develop a static deformation model that suggests with uniform initial channel geometry and no external loads, the actuated region of the developed soft

segments will deform under constant curvature. This differs from the above related work in the following ways.

1. It describes the deformation of a soft fluidic actuator that is a non-uniform cylindrical shape, operates at low pressures, and has a non-uniform cylindrical channel along the bending axis subject to unequal longitudinal and circumferential strain.
2. It accounts for the stress changing as a function of deforming channel geometry and is more valid for large deformations.
3. The model uses nonlinear material properties.

1.3. Overall contributions

Specifically, this paper contributes a novel autonomous three-dimensional fluidic elastomer manipulator. That is, we provide the following:

(a) a novel multi-segment manipulator prototype, (i) constructed 100% from soft silicone rubber, (ii) powered by four fluidic elastomer actuators per segment, and (iii) designed with a modular morphology suitable for automation;
(b) a novel process to repeatably fabricate this manipulator;
(c) a novel static model to understand a segment's deformation;
(d) a multi-segment kinematic model and processing and control systems that enable the first autonomous capabilities for this manipulator type, e.g. (i) following configuration trajectories within a sagittal plane and (ii) positioning in three-dimensions; also, without using the model and control system, we demonstrate (iii) advancing through a confined environment; and
(e) evaluations in both simulations and physical experiments.

This paper is organized as follows. In Section 2 we provide an overview of the aggregate soft fluidic elastomer manipulation system and introduce the major subsystems (i.e. actuation, perception, power, and processing and control). Section 3 presents the design, modeling, and fabrication of the soft spatial fluidic elastomer manipulator. Specifically, Section 3.1 describes the arm's morphology and Section 3.2 details alternative designs. In Section 3.3, we develop and experimentally validate a robot-dependent kinematic mapping to understand the deformation of the manipulator's individual segments as well as a multi-segment kinematic model based on the PCC assumption (Webster and Jones, 2010). In Section 3.4, we detail the fabrication process for the soft arm, which is a three-dimensional extension of a fabrication process the authors developed to construct a two-dimensional soft manipulator presented in Marchese et al. (2014a). Section 4 details the development of a high capacity fluidic drive cylinder array used to power actuation. Section 5 provides

a kinematic control algorithm for both measuring the arm's configuration and autonomously driving the arm to a user-specified target shape configuration. In Section 6 we explore new capabilities enabled by these above developments. We demonstrate how the kinematics and extreme compliance of such a soft manipulator enable it to fit within and advance through confined environments in Section 6.1. Next, we demonstrate how the continuum kinematics combined with our approach to closed-loop shape control enable the arm to conform to arbitrary configurations in real-time in Section 6.2. Lastly, in Section 6.3 we demonstrate it is feasible to position the soft fluidic elastomer manipulator in three dimensions.
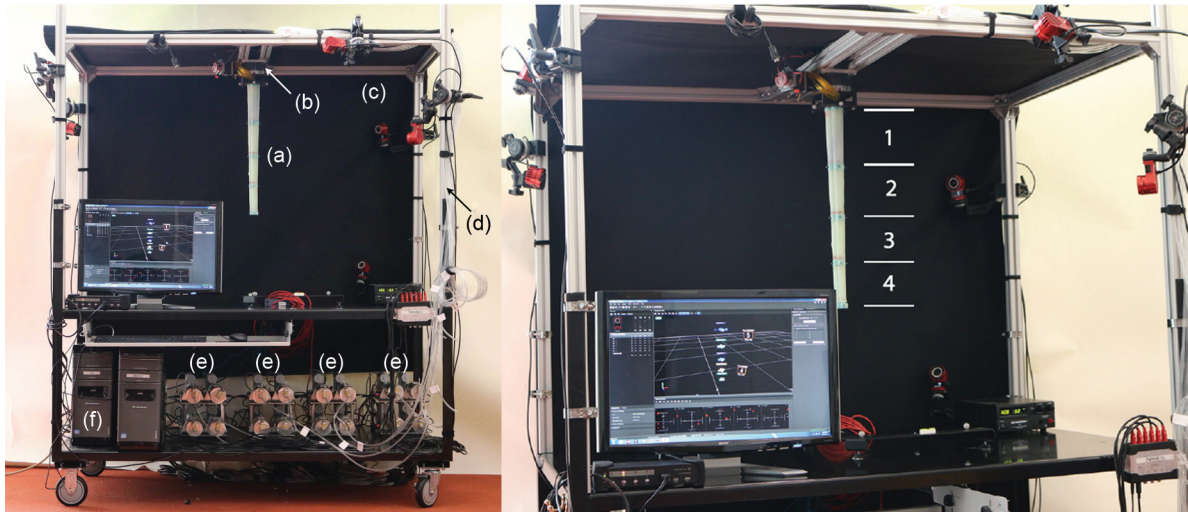
2. System overview

The soft fluidic elastomer manipulation system can move in three dimensions and is subject to gravity. The aggregate system is depicted in Figure 3 and contains actuation, perception, power, and computation subsystems. A fluidic elastomer arm composed entirely from soft silicone rubber is suspended (Figure 3(a)). Each of the manipulator's four body segments (Figure 3, 1–4) are independently actuatable with two bending DOFs and is fabricated through a multi-step casting process. The arm attaches to a grounded frame by means of a rotary stage at its base (Figure 3(b)). A bundle of transmission lines (Figure 3(d)) carries pressurized fluid from an array of fluidic drive cylinders (Figure 3(e)), or pumps, to actuated channels that are distributed throughout the arm. A system of cameras (OptiTrack; NaturalPoint, Inc., Corvallis, OR) (Figure 3(c)) is used to localize markers on the soft connectors between the arm's body segments. The computational subsystem (Figure 3(f)) uses kinematic algorithms and cascaded controllers to provide closed-loop curvature control of the manipulator. The subsystem determines the arms measured representation and target configurations as well as sends control signals to the fluidic drive cylinders.

3. Actuation

3.1. Soft manipulator design

The soft spatial manipulator is composed entirely from low durometer silicone rubbers and is actuated by pressurizing fluid channels embedded within the arm. The 50 cm long 600 g arm, shown in Figure 4(a), is composed of independently casted and serially concatenated modular segments that each move in three spatial dimensions with two DOFs. The arm is held horizontally from its midpoint subject to gravity emphasizing the manipulator's high body compliance in Figure 4(b). The durability of such an *entirely* soft design is shown in Figure 4(c)ã(e) as well as in Media Extension 1. These demonstrations are inspired by the resiliency tests that Tolley et al. (2014) use in the evaluation of a soft walking robot. The arm remains functional in extreme heat and in underwater environments while the

Fig. 3. Overview of the spatial fluidic elastomer manipulation system. The system consists of (a) soft spatial manipulator composed of four body segments, (b) rotary stage, (c) a system of cameras for external perception, (d) fluid transmission lines, (e) fluidic drive cylinders, and (f) processing and control algorithms.
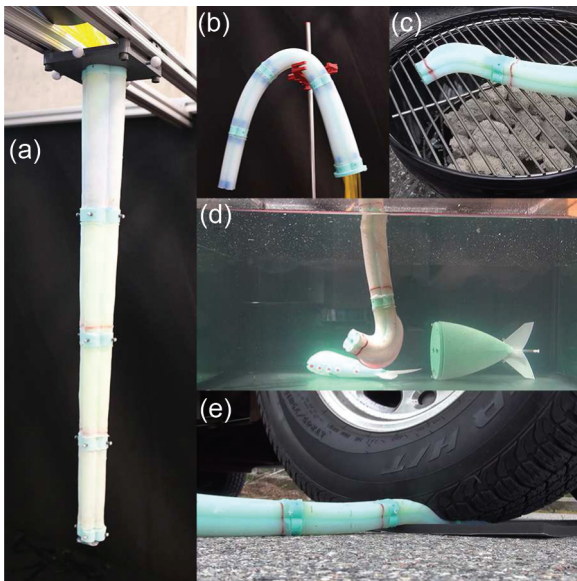

Fig. 4. (a) The soft spatial manipulator . Reproduced with kind permission from the IEEE (Marchese et al., 2015b); (b) the arm is suspended horizontally from its midpoint subject to gravity illustrating its high body compliance; (c) the arm is operated on the surface of a grill measuring 230°C; (d) the arm is operated under water; and (e) the arm is run over by a 4,000 kg truck at approximately 5 mph and afterwards resumes normal operation.

actuation system is placed external to the extreme condition. In addition, after being subjected to large compressive loads, the arm resumes normal operation. The same robot prototype used in these durability tests was used to perform all 42 reported experimental evaluations in the following sections. In total, this prototype withstood several hundred experimental evaluations.

The morphology of our spatial manipulator draws inspiration from previous work. The soft rubber tentacles developed by Martinez et al. (2013) use embedded pneumatic actuators in a similar two layer rubber construction. In addition, inspiration is drawn from a planar manipulator developed by the authors in Marchese et al. (2014a); however, the manipulator presented here differs from these works in several ways. Firstly, similar to our planar arm, this manipulator is modular in both design and fabrication; however, the spatial morphology differs in that each module or arm segment has four distributed fluidic actuators allowing it to move in three spatial dimensions. Secondly, similar to our planar design, but different from the design in Martinez et al. (2013), the manipulator presented here has features such as a hollow cylindrical interior and soft segment endplates. The hollow interior accommodates fluid transmission lines and allows modular assembly. The soft endplates contain markers allowing an external camera system to localize their positions. Both features are essential to an autonomous manipulation system. Thirdly, the arm has a longitudinally tapered and clover-shaped exterior (see Figure 5(b)) and this has a significant impact on the manipulator's dynamics (Marchese et al., 2015b) because of the reduced mass of the distal segments.

In Figure 5B, a schematic of the spatial manipulator is shown and as mentioned before, this manipulator is composed of four tapering segments separated by soft segment connectors (Figure 5(g)). Figure 5A depicts the two layer concentric structure of a segment. The outer layer (Figure 5(e)) is made from a very soft silicone rubber and the inner layer (Figure 5(d)) is made from a slightly stiffer silicone rubber. Within the outer layer of the segment, four cylindrical fluidic channels (Figure 5(c)) are embedded along the z-axis and are spaced at 90 intervals. These channels enable the arm to bend in two orthogonal planes. When a channel
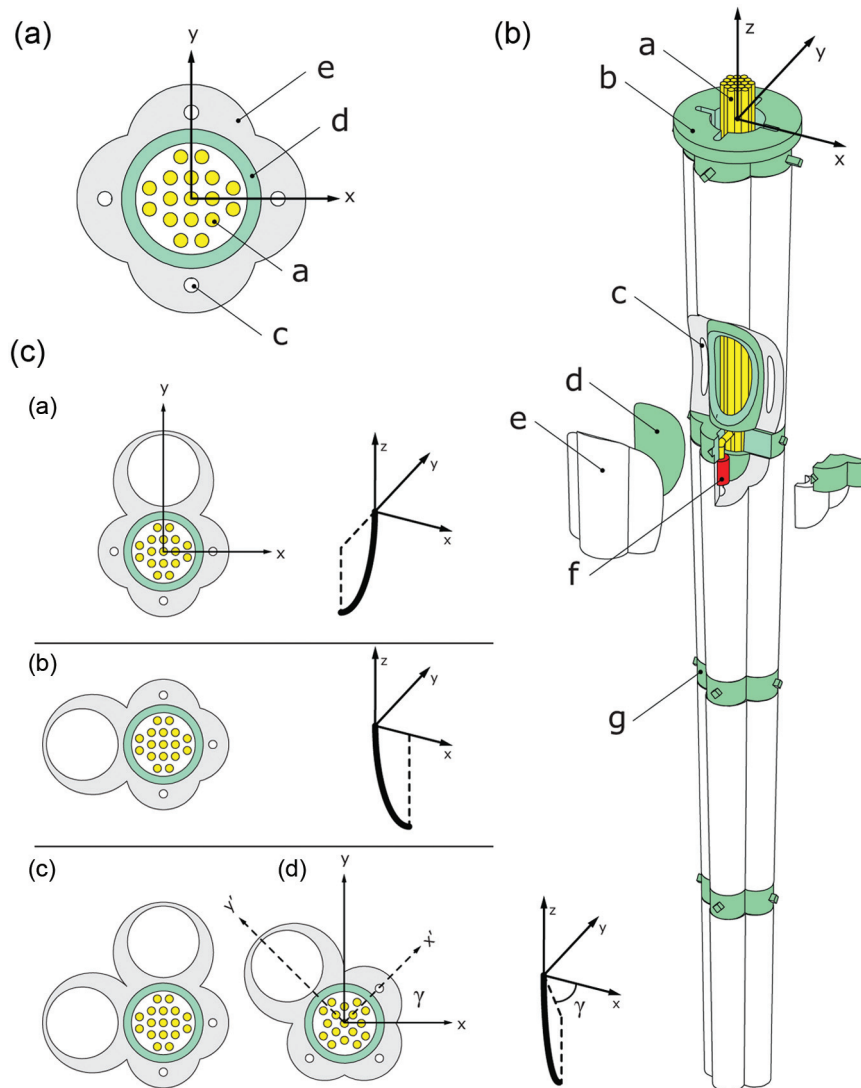
Fig. 5. (A) A cross-section in the *x–y* plane details the concentric layered structure of the manipulator's soft segments. (B) A schematic of the four segment spatial manipulator implemented in this work with the following components: (a) fluid transmission line bundle, (b) base connector, (c) expansion channels, (d) inner layer, (e) outer layer, (f) crush resistant channel inlet, and (g) segment connector. (C) The actuation motion primitives of a single soft segment: A segment bends through pressurization of the embedded fluidic channels.

is pressurized with fluid, the outer layer undergoes both longitudinal and circumferential strain; however, the inner layer is designed to be inextensible under the induced stresses and this difference in material strain results in bending about the inextensible *z*-axis. Bending motion primitives are shown in Figure 5(c). Combining actuation in the *x* and *y* directions allows for bending in any direction with zero rotation around the longitudinal axis. Alternatively, a traditional rotational DOF can be introduced at the segment's base to define γ and a single channel can be actuated to define κ. To achieve three-dimensional positioning, but to prevent the segments from twisting about their neutral axis (an unactuated DOF), in this work we actuate the manipulator in a sagittal plane defined by the rotation of a stage to which the base connector (Figure 5(b)) is mounted. Each segment's center is hollow and used to accommodate

internal fluid transmission lines (Figure 5(a)) that function to deliver pressurized fluid to each actuated channel as well as facilitate the concatenation of multiple segments. On one end, each transmission line is individually connected to each actuated channel in the multi-segment arm by means of a crush resistant silicone insert (Figure 5(f)) shown in red. These inserts are created from relatively stiff pieces of silicone tubing. On the other end, each line connects to the outlet of a fluidic drive cylinder, a device originally developed by the authors in Marchese et al. (2014b).

3.2. Alternative designs considered

To arrive at the current entirely soft manipulator design, we evaluated many alternative designs with varying degrees of rigidity. Through an iterative process, we were able to
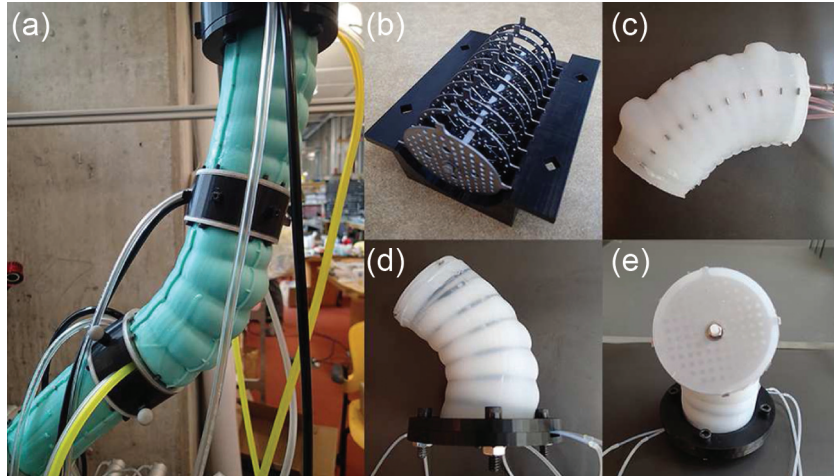
Fig. 6. Example design alternatives having varying degrees of rigidity. Through an iterative design process, all non-rubber components were removed.

design away all non-rubber components. For example, Figure 6 illustrates several of these past design alternatives. In Figure 6(a), a semi-soft manipulator is shown and it is composed of several arm segments each consisting of a plastic backbone and metal ribs surrounded by casted rubber (Figure 6(b)). Figure 6(c) shows one of these kinematically constrained soft segments under actuation. In this design iteration, the manipulator's endplates were rigid, and without a hollow interior, fluid transmission lines were run external to the manipulator. These lines interfered with the vision system's ability to measure marker locations as well as the manipulator's mobility. In addition, the arm segments shown here are cylindrical and uniform along the length of the manipulator producing a larger suspended mass than the current design. Figure 6(d) shows a second alternative design where a plastic helix was introduced around the segment's exterior. Noticeably, although this kinematic constraint reduced circumferential strain, it produced torsion about the neutral axis under actuation (Figure 6(e)).

3.3. Kinematic modeling

In order to autonomously perform tasks with the manipulator developed in Section 3.1, we must develop a multi-segment kinematic model. The objectives of this section are to:

(a) understand how an individual body segment deforms under fluidic input;
(b) determine what simplifying assumptions can be made in order to create a multi-segment kinematic model; and
(c) experimentally evaluate the proposed kinematic model.

An important result is that we use and validate a PCC modeling assumption (Webster and Jones, 2010), explained in

Section 1.2, to describe this multi-segment soft manipulator. The PCC-based kinematic model developed here will be used by a controller, detailed in Section 5, to regulate the manipulator's configuration in real-time.

3.3.1. Segment deformation. In this section we extend an analytical modeling approach presented by the authors in Marchese et al. (2014c) to understand how one of the manipulator's soft arm segments deforms. Although this deformation model is not utilized for any part of the controller, it is used as an analytical design tool for understanding how input pressure as well as physical actuator properties result in segment deformation. This simplified deformation model suggests that a significant portion of the actuator will deform under approximately constant curvature. Based on this observation, we use a simpler PCC model (see Section 3.3.5) to represent the manipulator's forward kinematics during control.

Figure 7 provides a schematic representation of a soft arm segment in both a neutral state (Figure 7(a)) and a deformed state (Figure 7(b)). In addition, Figure 7(c) illustrates an isometric view of a thin slice of the segment's elastically deformed outer layer.

The segment bends due to the relative difference in stiffness between the inner and outer rubber layers. The inner layer is cast from a rubber chosen to have an elastic modulus approximately 5.5 times greater than that of the outer layer, allowing us to make the assumption that the inner layer is inextensible relative to the outer layer. In addition, the outer layer thins considerably, further reducing stiffness. By pressurizing the fluidic channel embedded within the outer layer, stress is induced both circumferentially (normal to the neutral z-axis) and longitudinally (parallel to the neutral z-axis) in the outer layer, resulting in circumferential expansion and longitudinal elongation respectively. Due to the difference in lengths between the inner and outer layer, the segment bends.
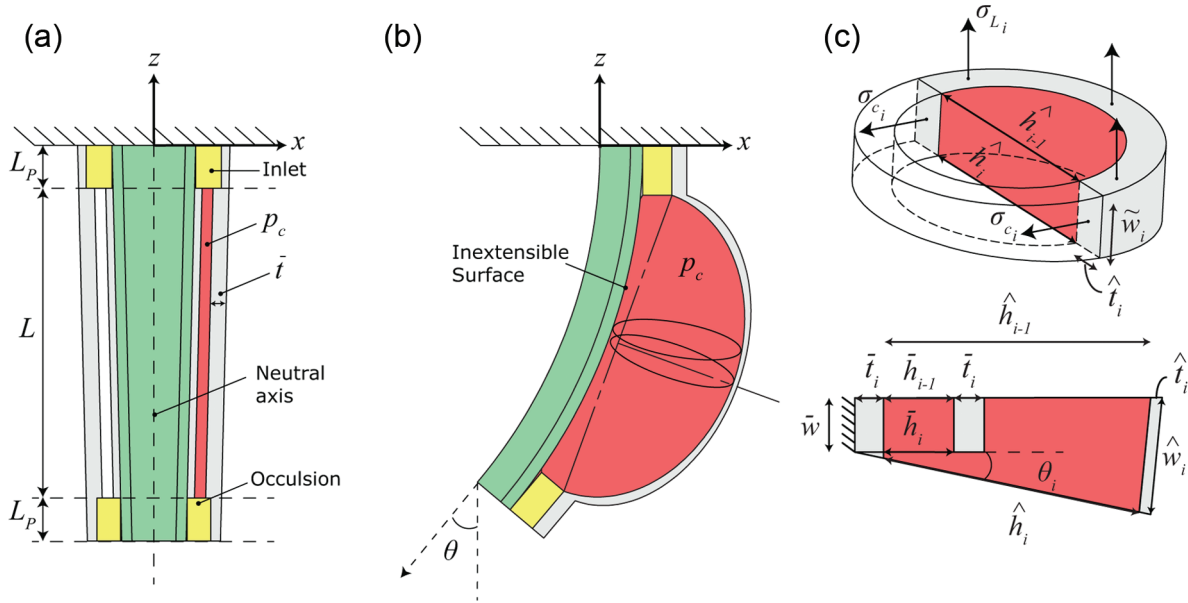
Fig. 7. Schematic representation of a soft arm segment under deformation.
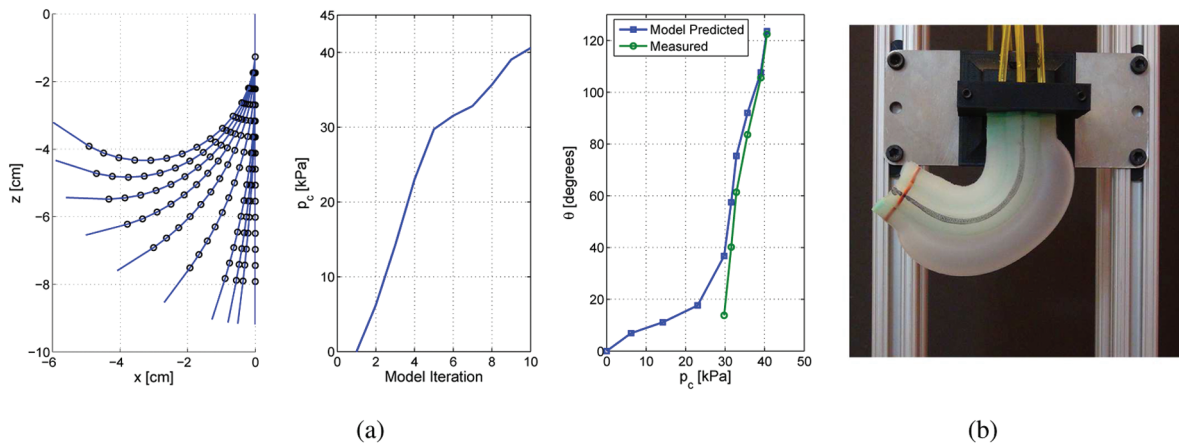

Fig. 8. (a) Left-hand side: neutral axis bending of the soft arm segment whose physical parameters are listed in Table 1 is simulated. Middle: details a priori channel pressure data successively input into the simulation each iteration. Right-hand side: the resulting model predicted and measured accumulated bending angle θ. (b) A photograph of the modeled segment at the maximum pressure used in the simulation.

In order to understand how a segment bends, we consider the case of one of the segment's channels deforming under pressure. Our approach is to first model the deformation of this channel as a function of the channel's fluid pressure p_c. The model is based on dividing the channel into J cross-sectional slices of uniform z-axis length cut parallel to the x–y plane and calculations are performed independently on each slice. In general, a bar ($^-$) is used to described an initial, undeformed channel dimension, whereas a hat ($\hat{}$) is used to describe a deformed channel dimension. Then, to simulate segment bending, we iteratively apply this model each time increasing p_c. More specifically, at each iteration the channel's circumferential and longitudinal deformed dimensions are recalculated based on the material stresses

that are derived from the previous iteration's deformed geometry. The model's input pressure p_c is not linearly increased, rather it is measured during a physical experiment where an actuator is incrementally filled under volume control (see Section 3.3.6). The motivation behind using this measured data as input is that it accounts for nonlinearities observed in the segment's pressure profile. Figure 8(a) depicts the bending of the inextensible layer predicted by the simulation as well as a priori channel pressure data that was successively input into the simulation at each iteration. Also, the measured, and the model predicted, accumulated bending angle θ is shown at each iteration. Figure 8(b) is a photograph of the actual segment that the model is based on at the maximum pressure used in the

Table 1. Segment parameters used in the simulation.

Parameter	Symbol	Value
Segment length	$L + 2L_P$	9.7 cm
Channel length	L	7.1 cm
Number of slices	J	15
Slice wall length	$\bar{w} = \frac{L}{J}$	0.47 cm
Channel diameter,	$\bar{h}$	0.32 cm
Channel wall thickness	$\bar{t}$	0.32 cm
Simulation iterations		10

simulation and experiment. Table 1 lists important model and simulation parameters.

3.3.2. Stresses and strains.

Stresses and strains in the elastomer can be approximated at a simulation iteration given the channel's current deformed geometry as well as the pressure input. After these stresses and strains are computed, they can be used to update the channel's deformed geometry for the next simulation iteration. First, we find the material stresses. Due to the fact that each of the segment's embedded channels are cylindrical, we can approximate the circumferential stress σ_c in a thin cross-sectional channel slice by balancing static forces. That is, the pressure force acting to circumferentially expand the channel should balance with the product of circumferential wall stress and wall area (see Figure 7(c) for visualization)

$$2\,\sigma_{c_i}\,\hat{t}_i\,\tilde{w}_i \approx p_c\,\frac{\hat{h}_{i-1} + \hat{h}_i}{2}\,\tilde{w}_i \quad \forall i = 1, \ldots, J \quad (1)$$

$$\sigma_{c_i} \approx p_c\,\frac{\hat{h}_{i-1} + \hat{h}_i}{4\,\hat{t}_i} \quad \forall i \quad (2)$$

When the condition $\hat{h}_{i-1} = \hat{h}_i$ is met,

$$\sigma_{c_i} \approx p_c\,\frac{\hat{h}_{i-1}}{2\,\hat{t}_i} \quad \forall i \quad (3)$$

In the above approximations, i is the slice index, J is the total number of slices, p_c is the channel's fluid pressure, and $\hat{h}$, $\hat{w}$, and $\hat{t}$ are a slice's deformed channel diameter, distal wall length, and wall thickness, respectively. The dimension $\tilde{w}$ represents the slice's deformed wall length midway through the slice (see figure 7(c)).

Using a similar approach to determining the circumferential stress, we can approximate the longitudinal stress σ_L in a slice as

$$\sigma_{L_i} \approx \frac{p_c\,\hat{h}_{i-1}^2}{4b\,\hat{t}_i\left(\hat{t}_i + \hat{h}_{i-1}\right)} \quad \forall i = 1, \ldots, J \quad (4)$$

To arrive at the above approximation (equation (4)), we include a free parameter b allowing the stress to be adjusted such that the model predictions better match experimentally observed deformations. It is important to note that this
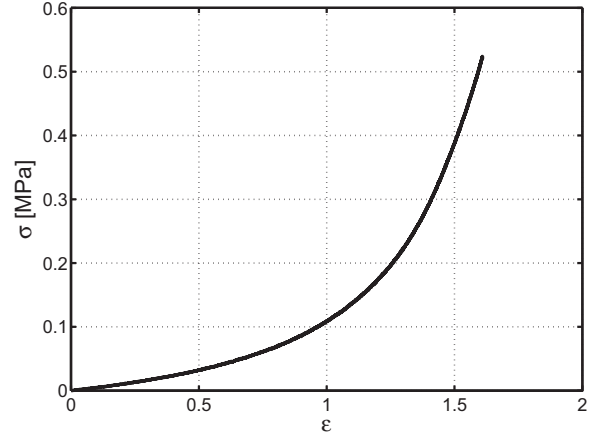
Fig. 9. True stress true strain relationship of the rubber material composing a segment's outer layer.

is the only free parameter in the model. We use $b = 4$ and justify this by using the fact that the inner most portion of the channel wall is laminated to an inextensible surface, counteracting a significant portion of the applied pressure force. An important insight from this is that the longitudinal stress is predicted to be approximately one eighth of the circumferential stress.

Next, the circumferential and longitudinal strain, ϵ_c and ϵ_L respectively, can be determined using a look-up table based on the material's measured true stress true strain relationship, shown in Figure 9.

3.3.3. Updating channel geometry.

Having determined the material's strain, we can now update the deformed dimensions of a channel slice under the increased pressure. That is, the elongated wall $\hat{w}$, the expanded diameter $\hat{h}$, and compressed thickness $\hat{t}$ can be expressed using the calculated material strain, the initial channel geometry (represented by $\bar{h}$, $\bar{w}$, and $\bar{t}$), and the conservation of material volume as silicone rubber is incompressible. The dimension $\hat{w}$ is updated according to

$$\hat{w}_i \approx \bar{w}_i\left(\epsilon_{L_i} + 1\right) \quad \forall i \quad (5)$$

The updates for $\hat{h}$ and $\hat{t}$ can be found by solving a system of two equations. Equation (6), is found using the previously determined circumferential strain,

$$\hat{h}_i \approx \frac{\hat{c}_i}{\pi} - \hat{t} \quad \forall i \quad (6)$$

where

$$\hat{c}_i \approx \bar{c}_i\left(\epsilon_{c_i} + 1\right) \quad (7)$$

$$\bar{c}_i = \pi\left(\bar{h}_i + \bar{t}_i\right) \quad (8)$$

The dimensions $\bar{c}$ and $\hat{c}$ represent the undeformed and deformed channel circumference measured half-way through the wall's thickness. Equation (9), is found using the conservation of material volume. That is, the initial

volume of elastic material in a slice is equal to the volume of material in the slice when it is deformed

$$\bar{A}_i \, \bar{w}_i \approx \hat{A}_i \, \bar{w}_i + \hat{A}_i \, \frac{\hat{w}_i - \bar{w}_i}{2} \quad \forall i \qquad (9)$$

where $\bar{A}$ and $\hat{A}$ are the initial and deformed cross-sectional area of a slice, respectively. More specifically

$$\bar{A}_i = \pi \left(\frac{\bar{h}_i}{2} + \bar{t}_i \right)^2 - \pi \left(\frac{\bar{h}_i}{2} \right)^2 \quad \forall i \qquad (10)$$

$$\hat{A}_i = \pi \left(\frac{\hat{h}_i}{2} + \hat{t}_i \right)^2 - \pi \left(\frac{\hat{h}_i}{2} \right)^2 \quad \forall i \qquad (11)$$

According to the technique outlined in the actuation section of Marchese et al. (2014c), the accumulated angle θ along the neutral axis at this simulation iteration is

$$\theta = \sum_{i=1}^{J} \cos^{-1} \left(\frac{-\hat{w}_i^2 + \hat{h}_{i-1}^2 + \bar{w}^2 + \hat{h}_i^2}{2\hat{h}_i \sqrt{\hat{h}_{i-1}^2 + \bar{w}^2}} \right) - \tan^{-1} \left(\frac{\bar{w}}{\hat{h}_{i-1}} \right) \qquad (12)$$

3.3.4. Conditions for constant curvature. From this model we can make the following observation: if the initial undeformed channel dimensions are constant along the length of the channel, i.e.

$$\bar{w}_i = C_1 \quad \forall i = 1 \ldots J \qquad (13)$$

$$\bar{h}_i = C_2 \quad \forall i \qquad (14)$$

$$\bar{t}_i = C_3 \quad \forall i \qquad (15)$$

then the deformed dimensions $\hat{w}$, $\hat{h}$, and $\hat{t}$ and accordingly the bending angle θ are constant $\forall i = 2, \ldots, J-1$ along the length of the channel.

It is important to note that under these simplified conditions, only the actuated region of the segment, i.e. the channel with arc length L (see Figure 7), is expected to deform under constant curvature; both the channel inlet region as well as the channel occlusion region contribute nonconstant curvature effects to the aggregate segment's bending profile because of the increased stiffness in these regions. To account for this, linear transformations are added before and after the constant curvature transformation in equation (16) within Section 3.3.5.

3.3.5. Segment transformation. Given that a channel deforms under approximately constant curvature, we can write the following transformation from the base of a segment to the tip

$$\mathbf{S}_{\text{tip}}^{\text{base}} = \mathbf{R}_z(\gamma) \, \mathbf{T}_z(L_P) \, \mathbf{R}_y \left(\frac{\theta}{2} \right) \mathbf{T}_z(d(\theta)) \, \mathbf{R}_y \left(\frac{\theta}{2} \right) \mathbf{T}_z(L_P) \qquad (16)$$

Here, $\mathbf{T}$ and $\mathbf{R}$ represent coordinate translations and rotations along and about the subscript axes; refer to Figure 7 for coordinate definitions. The center three transformations are consistent with kinematic representations of continuum manipulators, and are used when the constant curvature assumption is valid (Webster and Jones, 2010). In the context of this work we need to add additional translations along z before and after the bent channel to account for the relative rigidity of the inlet pieces. In addition, we redefine $d(\theta)$ with an approximation that is singularity free for the reason of numerical stability

$$d(\theta) = \frac{2L}{\theta} \sin \left(\frac{\theta}{2} \right) \qquad (17)$$

$$d(\theta) \approx L \left(a\,\theta^2 - 1 \right) \qquad (18)$$

where a is a fitting coefficient. An important observation is that the segment transformation $\mathbf{S}_{\text{tip}}^{\text{base}}$ has two DOFs. That is, if we know the sagittal plane along which the segment is bending, specified by γ, and are given one point along the segment's neutral axis in reference to the segment's base we can uniquely define θ. In addition, in order to specify a point along the neutral axis of the curved region $s = [0, L]$ in reference to the base of the channel we use the following transformation

$$\mathbf{S}_{s}^{\text{base}} = \mathbf{R}_z(\gamma) \, \mathbf{T}_z(L_P) \, \mathbf{R}_y \left(\frac{\kappa s}{2} \right) \mathbf{T}_z(d(\kappa s)) \mathbf{R}_y \left(\frac{\kappa s}{2} \right) \atop \kappa = \frac{\theta}{L} \qquad (19)$$

The kinematics of a multi-segment soft arm composed of N segments can be represented by cascading single segment transformations together

$$\mathbf{M}_{\text{tip}_N}^{\text{base}} = \mathbf{S}_{tip}^{\text{base}}(\gamma_1, \theta_1) \, \mathbf{S}_{\text{tip}}^{\text{base}}(\gamma_2, \theta_2) \cdots \mathbf{S}_{\text{tip}}^{\text{base}}(\gamma_N, \theta_N) \qquad (20)$$

3.3.6. Model evaluations. In order to validate this kinematic model we fabricated and actuated the segment described physically in Table 1 subject to gravity. The segment weighs 65 grams. The primary concept we are evaluating in this experiment is: if we identify a single point on the arm segment, i.e. the tip, and the segment's base position and orientation is known, then we can uniquely define the entire segment's neutral axis. The experiment consists of incrementally filling a single channel with between 0 and 70 ccm of air and photographing the segment's deformation. As a metric of goodness of fit, we compare our models predicted bending angle θ^P with the measured bending angle θ^M at each incremental fill level. In addition, we compare our models predicted center of gravity G^P with the measured center of gravity G^M. Measurements were taken along the neutral axis of the segment using image analysis. θ^M was measured from the unbent tip region and G^M was taken to be at $s = L/2$, the center point of the neutral axis. The model is defined using a single point, in this case the segment's tip. Figure 10(a) shows the test segment
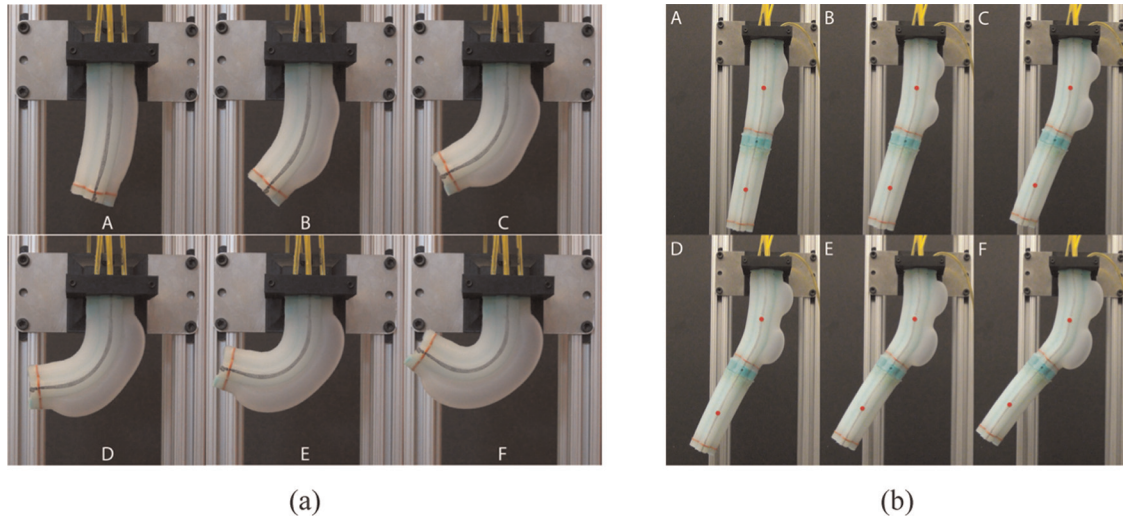
Fig. 10. Experimental validation of the proposed segment transformation. (a) A single segment is incrementally filled with air in the sequence of images (A–F). (b) A larger soft segment is actuated in the image sequence (A–F) with the suspended weight of a second distally attached segment.

Table 2. Comparison between the measured and the model predicted deformation kinematics.

Fig 10(a)	Volume (ccm)	Pressure (kPa)	θ^P (°)	θ^M (°)	$|G^P - G^M|$ (cm)
(F)	72	40.6	121	122.5	0.54
(E)	64	39.0	104	105.6	0.45
(D)	56	35.7	83	83.6	0.48
(C)	48	32.8	61	61.4	0.30
(B)	40	31.5	39	40.2	0.20
(A)	32	29.7	16	13.8	0.24

**Table 3.** Comparison between measured and model predicted deformation kinematics for segment under external load

Fig 10(b)	Volume (ccm)	Pressure (kPa)	θ^P (°)	θ^M (°)	$|G^P - G^M|$ (cm)
(F)	72	40.6	33.1	39.9	0.30
(E)	64	39.0	28.3	34.5	0.18
(D)	56	35.7	24.4	28.1	0.12
(C)	48	32.8	19.2	20.5	0.03
(B)	40	31.5	14.6	15.3	0.09
(A)	32	29.7	9.9	10.0	0.08
-	24	23.0	4.3	3.7	0.09

being incrementally filled from 32 to 72 ccm of air. Table 2 contains a comparison between measured and model predicted deformation kinematics.

In addition, we performed the same experiment on a segment weighing 173 grams under the external load of an attached second segment weighing 85 grams. The intent of this experiment was to quantify the error in the proposed kinematic segment model when the segment is under significant external load. For the same volumetric input, the maximum measured bending angle of 40° is significantly smaller than in the unloaded case, 123°. As expected, the error in the model predicted bending angle is higher in the loaded case than in the unloaded case and in the loaded case the error increases with gravitational loading. Within the range ±40° the error does not exceed 7.0°, with a mean of 2.7°. Figure 11 depicts the percent error in the prediction as a function of measured bending angle. Generally, as bending angle increases the error in predicted bending angle grows. Figure 10(b) shows the loaded test segment being incrementally filled from 32 to 72 ccm of air.

3.3.7. Limitations. The static deformation model is most valid for describing the soft segment's deformation at larger
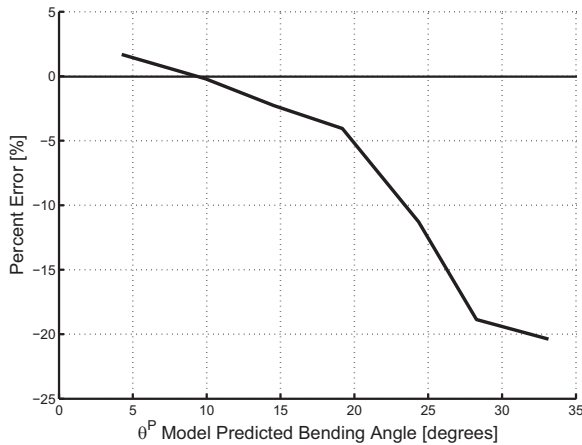
Fig. 11. The percent error in the model predicted bend angle as a function of model predicted bending angle θ^P

Fig. 12. A characterization of the base segment's blocking force.

bend angles. At lower pressures, the model predicted and measured bend angles deviate significantly. This is likely because the presented model does not capture the bi-stable, nonlinear channel deformation encountered when inflating a thin-walled elastomer tube (detailed in Gent (2012)). A more detailed explanation of this phenomenon and how it relates to the actuator's performance can be found in Section 6.2.3. However, it is possible that by adjusting the model's free parameter b at each iteration, such nonlinear behavior can be more closely approximated.

A notable limitation in our experimental evaluation of the developed kinematic model is that we do not directly establish the validity of the PCC-based model's ability to describe the backbone's continuous deformation; rather we experimentally validate the model's ability to describe the segment's aggregate bend angle and center of mass location, which are indirectly a function of the continuous deformation.

In addition, the developed soft segments have physical limitations. For example, they are inherently force limited and this impacts the maximum achievable bend angle of a segment. In Section 3.3.6 the manipulator's second segment was actuated while the third segment (having a mass equal to approximately 50% of the second) was secured to the tip. The maximum achievable bend angle was limited to approximately 40°. Although smaller in size, when the same fluidic displacement was delivered to the manipulator's fourth segment free of external loads, a maximum bend angle of approximately 120° was achieved.

To characterize this force output limitation, we performed a blocking force experiment and this is detailed in Figure 12. Here, the manipulator's base segment, segment one, is isolated and actuated against a restraint at its tip. The segment's base is securely fixed and the restraint is in the form of a cable coupled to a force transducer. A fluidic drive cylinder (see Section 4) is used to incrementally vary the volume of air in the soft segment's agonistic channel and this displacement is measured by means of a linear
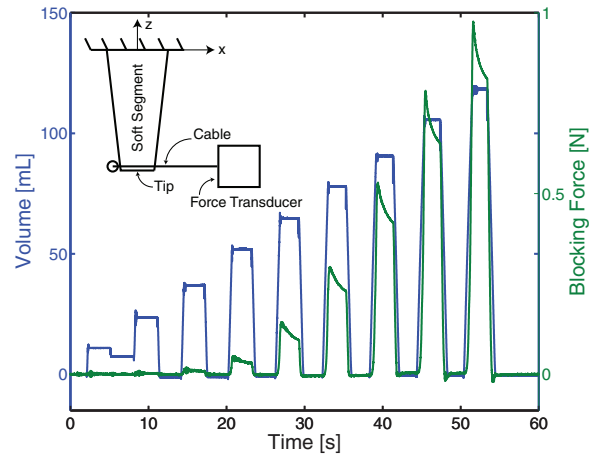
Table 4. Fabrication tools and materials

|	
1	Fortus 400mc, Stratasys Ltd., Eden Prairie, MN
2	Ecoflex 0030, Smooth-On, Easton, PA
3	AL Cube, Abbess Instruments and Systems, Inc., Holliston, MA
4	Mold Star 15, Smooth-On, Easton, PA
5	Silicone Sealant 732, Dow Corning Corp, Midland, MI
6	PN 51845K52, McMaster, Princeton, NJ

potentiometer. As shown in Figure 12, each time the drive piston was incrementally displaced, the piston was held for several seconds and then returned to its initial position. This pattern allowed us to observe the actuator's elastic hysteresis, which is likely caused by the non-hookean behavior of the rubber material. When the rubber is subject to high rates of strain (i.e. high volumetic flow rates), the material exhibits increased stiffness and more effectively transfers input fluid energy into actuator tip force. Then, when the load is constant (i.e. the piston's position is held constant), the elastomer exhibits a decrease in stiffness and accordingly the actuator's channel expands under the fluid energy lessening the actuator's tip force.

3.4. Manipulator fabrication

The fabrication process for this spatial soft arm is a three-dimensional extension of a fabrication process the authors developed to construct a planar soft manipulator presented in Marchese et al. (2014a). The tools and equipment used for fabrication are listed in Table 4. Generally, we fabricate the arm through a casting process that uses pourable silicone rubber[2,4] and three-dimensional printed molds[1]. Figure 13 and Algorithm 1 detail the fabrication process for the spatial manipulator. The general approach is to first independently cast each segment and connector in steps (1)–(5) and subsequently join these segments serially to

Algorithm 1. Fabrication process (See Figure 13).

Result: A multi-segment soft manipulator
Repeat

1	Assemble and prepare mold (step 1).
2	Pour soft rubber[2] to cast segment's outer layer (step 2).
3	Remove sleeve to create inner cavity (step 3).
4	Pour stiffer rubber[4] to cast segment's inner layer and connector piece (step 4).
5	Demold and attach[5] transmission lines and connector piece to segment (step 5).

   until *All N segments are complete*
6   Join *N* segments together using adhesive[5] to form manipulator.
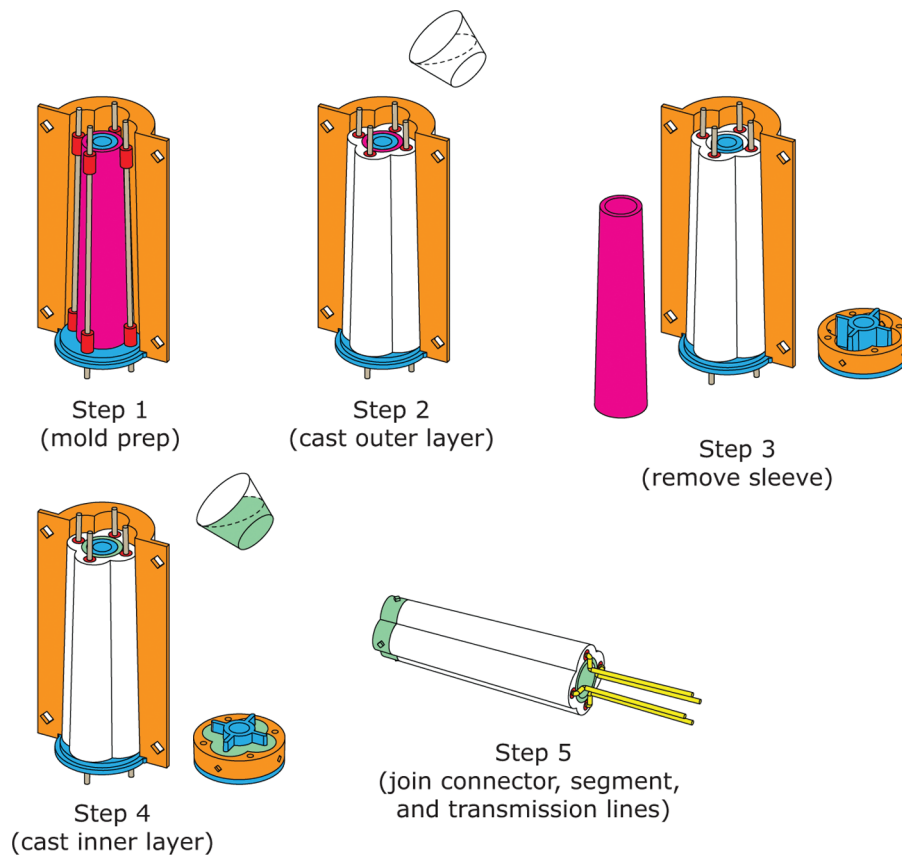

Fig. 13. A sequence of pictures depicting the five step casting process used to fabricate a soft spatial arm segment. A mold is prepared in step 1 and poured in steps 2–4. In step 5 the segment is demolded and transmission lines as well as a connector piece are attached.

form the manipulator. Prior to the process, a four piece mold was designed and printed. The mold consists of: (1) a two-part outer shell (Figure 13 *orange*) that functions to form the segment's clover-like exterior, (2) the mold's interior piece (Figure 13 *blue*) that functions to produce the body's hollow interior, (3) metal rods (Figure 13 *grey*) inserted into the interior piece to form cavities for the segment's four embedded pneumatic channels, and lastly (4) a removable sleeve (Figure 13 *fuchsia*).

In step 1, the four mold parts are assembled and eight crush resistant silicone pieces (Figure 13 *red*) are slid over the metal rods. These relatively stiff pieces will eventually form inlets to the embedded channels. All inlet pieces are

cut to length and cleaned with rubbing alcohol to ensure a good bond between their surface and the later introduced silicone rubber. To prepare four molds for the parallel casting of four segments, this step takes approximately one hour. In step 2, a low elastic modulus rubber[2] is mixed, degassed in a vacuum chamber[3], and poured to form the body segment's soft outer layer (Figure 13 *white*). The rubber is poured slowly into the top of the mold. Because the material gradually thickens as a function of time (i.e. a pot life of 45 minutes), we often mix and pour two sequential batches of rubber to ensure the material remains at a sufficiently low viscosity to enter the mold. When pouring four molds in parallel, this stage of the process can take between
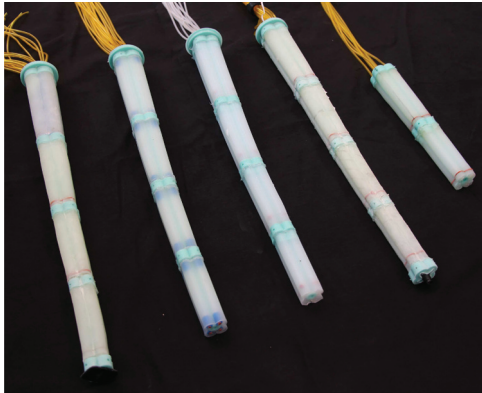
Fig. 14. Functional soft fluidic elastomer manipulators fabricated using the process outlined in Figure 13 and Algorithm 1.

one and two hours depending on experience. Once the outer layer has fully cured (four hours), the mold is disassembled and the rigid *fuchsia* sleeve is removed in step 3. When the mold and outer layer are reassembled, this produces a cavity between the outer layer (Figure 13 *white*) and interior mold piece (Figure 13 *blue*). Also, we prepare a smaller separate mold for the segment's connector. This step takes approximately one to one and a half hours while preparing four segments. In step 4, we pour a slightly stiffer rubber[4] into this newly formed cavity and this forms the segment's partially constraining inner layer (Figure 13 *green*). Simultaneously, we pour the segment's connector, also shown in *green*. The mixing and pouring process is identical to that in step 2 and this stage can also take between one and two hours depending on experience. During step 5 the pieces are removed from their molds, cleaned, and the segment is joined to the rubber connector using adhesive[5]. Also, soft rubber tubes[6] (Figure 13 *yellow*) are used for transmission lines and are joined to the channel's inlets. To make four segments, this step takes approximately 2 and a half hours. Lastly, to assemble the manipulator in step 6 the transmission line bundle is passed through each segment's hollow interior and the segments are joined together using the same silicone adhesive.

This fabrication process was used to make four complete, functional soft manipulators (see Figure 14) and numerous individual segments not shown. For each prototype, minor variations in the manufacturing process were evaluated, but fundamentally each fabrication cycle is represented by the six step process outlined above. One variation to this process included casting the inner layer in a separate mold a priori and then using this in place of the removable sleeve to eliminate intermediate demolding.

4. Power

The soft manipulator is powered by pressurized fluids, specifically we use air because of its low viscosity. This feature presents the unique challenges of (1) needing to supply each of the manipulator's actuators with a continuous
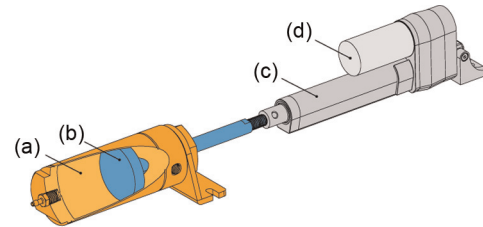

Fig. 15. Top: schematic representation of a high capacity fluidic drive cylinder. The device consists of a (a) fluidic cylinder, (b) piston, (c) linear drive, and (d) electric motor. Bottom: An array of 16 fluidic drive cylinders used to power the spatial soft arm. Reproduced with kind permission from the IEEE (Marchese et al., 2015b)

source of fluid energy for prolonged operation and (2) needing the ability to continuously adjust input energy for smooth curvature control. To address these challenges we constructed an array of 16 fluidic drive cylinders, detailed in Figure 15, and these serve to individually pressurize each of the manipulator's embedded channels. We conceived and implemented a smaller version of the fluidic drive cylinder array in previous work (Marchese et al., 2014b); however, both the maximum achievable flow rate and maximum volumetric capacity of the original array were insufficient for the functional requirements of the larger spatial manipulation system, necessitating the array to be redesigned. Each cylinder maps one-to-one with an actuated channel, and agonist-antagonist pairs of actuators are pressurized by a pair of cylinders driven in sequence.

The fluidic drive cylinder has several advantages when compared to other fluidic energy supplies (e.g., rotary pumps (Katzschmann et al., 2014) and compressed gas (Marchese et al., 2014c)):

(a) the segment curvature is monotonically related to cylinder displacement;
(b) the drive system is closed-circuit meaning a constant volume of transmission fluid is moved around the system and none is intentionally exhausted to the environment; and,
(c) the flow can be continuously adjusted.

These advantages enable real-time curvature control, as initially demonstrated in Marchese et al. (2014b), as well as the prolonged operation of the manipulation system. In
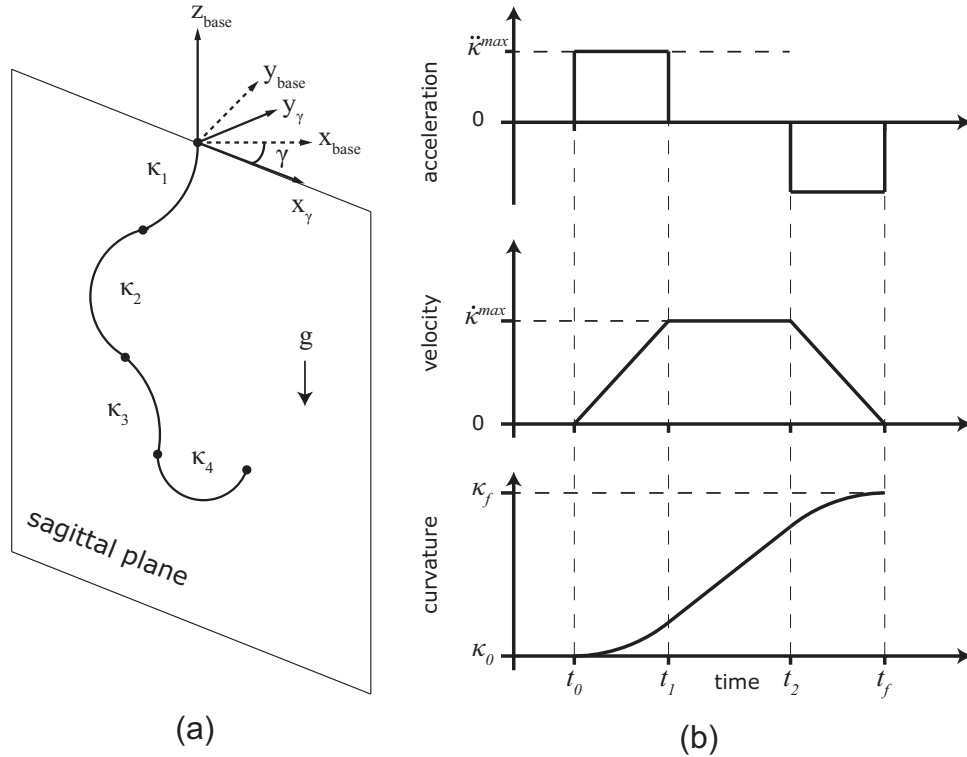
Fig. 16. (a) A simplified state representation of the soft fluidic elastomer manipulator using PCC modeling (Webster and Jones, 2010) rationalized and experimentally validated in the context of this arm in Section 3.3. The simplifying assumptions of this model include: (1) the N arm segments bend according to constant curvature within a sagittal plane defined by the rotation $\mathbf{R}_z(\gamma)$ of a base frame and (2) the lengths of the passive portions of each segment are negligible, i.e. $L_P \to 0$. (b) A realizable reference curvature trajectory generated by the controller (Algorithm 2) is shown for a single segment. The trajectory is computed under the constraints of (1) a trapezoidal velocity profile as well as (2) empirical constraints on acceleration and velocity, $\ddot{\kappa}^{\mathrm{max}}$ and $\dot{\kappa}^{\mathrm{max}}$ respectively.

addition, it is important to note that the product of change in the pressure and change in volume is likely a better representation of the soft actuator's state, but in our current control approach we have found it sufficient to simply use volume change as a control variable.

Specifically, each fluidic drive cylinder consists of several components: a nose-mounted, 63.5 mm bore, 76.2 mm stroke air cylinder (PN 503-D; Bimba Manufacturing Company, University Park, IL) shown in Figure 15(a) and (b); a 12 V, 100 mm stroke, 43 mm/s electric linear actuator (PN 2319; Pololu Corporation, Las Vegas, NV) shown in Figure 15(c) and (d), as well as a positional controller for these linear actuators (PN 1393; Pololu Corporation).

5. Processing and control

In order to autonomously control the spatial manipulator's configuration in real-time, we develop a kinematic controller. The controller (see Algorithm 2) performs several tasks: Firstly, the procedure `generateTraj()` generates a realizable curvature velocity trajectory $\dot{\boldsymbol{\kappa}}(t)$ that takes the arm's segments from their initial state $\boldsymbol{\kappa}_0$ at $t = t_0$ to a desired state $\boldsymbol{\kappa}_f$ at $t = t_f$ (see Figure 16(b)). This velocity trajectory is trapezoidal and computed from empirically

determined constraints on acceleration and velocity, $\ddot{\boldsymbol{\kappa}}^{\mathrm{max}}$ and $\dot{\boldsymbol{\kappa}}^{\mathrm{max}}$ respectively. Secondly, the procedure `driveSegments()` physically advances the arm segments along the aforementioned trajectory under closed-loop control. More specifically, when a new measurement is available from the marker-based vision system (OptiTrack; NaturalPoint, Inc., Corvallis, OR) segment endpoints are identified in reference to a base frame (i.e. $\mathbf{E}_n^{\mathrm{base}} \subset \mathbb{R}^3 \quad \forall n = 1, \ldots, N$) and subsequently transformed into the manipulator's sagittal plane (i.e. $\mathbf{E}_n^{\gamma} \subset \mathbb{R}^2 \quad \forall n = 1, \ldots, N$) specified by the rotation γ. Next, these endpoints are used to determine the manipulator's measured curvature configuration representation $\boldsymbol{\kappa}_{\mathrm{meas}}$ at the current instant in time (see Figure 16(a)). This stage is accomplished using a geometric algorithm referred to here as `singleSegInvKin()` and developed by the authors in Marchese et al. (2014b). This procedure computes the inverse kinematics of a single planar segment. That is, given the start and end points of a segment as well as its starting orientation we can uniquely determine its signed curvature. Next, a reference configuration $\boldsymbol{\kappa}_{\mathrm{target}}$ is computed from the realizable reference trajectory $\dot{\boldsymbol{\kappa}}(t)$ at the current instant in time. The computed error then becomes the input to an array of cascaded PI-PID

Algorithm 2. Configuration controller.

Input: $\boldsymbol{\kappa}_0$, $\boldsymbol{\kappa}_f$, $\dot{\boldsymbol{\kappa}}^{\max} > \mathbf{0}$, $\ddot{\boldsymbol{\kappa}}^{\max} > \mathbf{0}$, γ
Result: Manipulator moves along configuration trajectory from $\boldsymbol{\kappa}_0$ to $\boldsymbol{\kappa}_f$.
1   $\dot{\boldsymbol{\kappa}}(t) \leftarrow$ generateTraj$\left(\boldsymbol{\kappa}_0, \boldsymbol{\kappa}_f, \dot{\boldsymbol{\kappa}}^{\max}, \ddot{\boldsymbol{\kappa}}^{\max}\right)$
2   driveSegments$(\dot{\boldsymbol{\kappa}}(t), \gamma)$

    Procedure `generateTraj`$(\boldsymbol{\kappa}_0, \boldsymbol{\kappa}_f, \dot{\boldsymbol{\kappa}}^{max}, \ddot{\boldsymbol{\kappa}}^{\max})$
      Result: $\dot{\boldsymbol{\kappa}}(t)$ that takes segments from $\boldsymbol{\kappa}_0$ at $t = t_0$ to $\boldsymbol{\kappa}_f$ at $t = t_f$
      for $n = 1 \dots N$. **do**
        All κ in this loop are indexed by i but omitted for convenience

        if $\left|\kappa_f - \kappa_0\right| < 2\frac{(\dot{\kappa}^{\max})^2}{\ddot{\kappa}^{\max}}$ **then**
          $\dot{\kappa}^{\max} \leftarrow \text{SGN}\left(\kappa_f - \kappa_0\right)\sqrt{\left|\kappa_f - \kappa_0\right|\ddot{\kappa}^{\max}}$.

          $t_1 \leftarrow \frac{\left|\kappa_f - \kappa_0\right|}{\left|\dot{\kappa}^{\max}\right|}$.

          $t_2 \leftarrow t_1$.

        else

          $\dot{\kappa}^{\max} \leftarrow \text{SGN}\left(\kappa_f - \kappa_0\right)\dot{\kappa}^{\max}$.

          $t_1 \leftarrow \frac{\left|\dot{\kappa}^{\max}\right|}{\ddot{\kappa}^{\max}}$.

          $t_2 \leftarrow \frac{\left|\kappa_f - \kappa_0\right|}{\left|\dot{\kappa}^{\max}\right|}$.

        end
        $t_f \leftarrow t_1 + t_2$.

        $\mathbf{t} \leftarrow [0, t_1, t_2, t_f, t_f + \epsilon]$.

        $\mathbf{v} \leftarrow [0, \dot{\kappa}^{\max}, \dot{\kappa}^{\max}, 0, 0]$.

        $\dot{\kappa}(t) \leftarrow$ firstOrderHold$(\mathbf{t}, \mathbf{v})$.
      end
    return $\dot{\boldsymbol{\kappa}}(t)$
    Procedure `driveSegments`$(\dot{\boldsymbol{\kappa}}(t), \gamma)$
      Result: Drive segments to desired configuration
      $t \leftarrow t_0$.
      while $t < max(t_f)$ **do**
        if *A new sensor measurement* $\mathbf{E}^{base}$ *is available* **then**

          $\mathbf{E}_n^{\gamma} \leftarrow \left[\mathbf{T}_{\gamma}^{\text{base}}(\gamma)\right]^{-1}\mathbf{E}_n^{\text{base}} \quad \forall n = 1\,N$.

          $\boldsymbol{\kappa}_{\text{meas}} \leftarrow$ `singleSegInvKin`$(\mathbf{E}^{\gamma})$ (Marchese et al., 2014b).

          $\kappa_{\text{target}} \leftarrow \int_{t_0}^{t} \dot{\kappa}_n(t)\,\mathrm{d}t \quad \forall n$.

          Send error $(\boldsymbol{\kappa}_{\text{target}} - \boldsymbol{\kappa}_{\text{meas}})$ to low level cascaded PI-PID controllers (Marchese et al., 2014b).
        end
        $t \leftarrow$ elapsed time.
   **end**
    return

(curvature and cylinder displacement, respectively) controllers, a control strategy developed by the authors in Marchese et al. (2014b).

6. Capabilities

6.1. Confined environment

The kinematics and extreme compliance of an entirely soft manipulator enable it to fit within and advance through confined environments. The goal of this section is to compare the ability of a soft continuum robot and rigid discrete robot to passively advance through a curved environment. Consider the task of conforming to an environment whose boundaries can be parameterized by curved cylinders or tubes. For a manipulator operating in such an environment, we define the minimum confining space $\hat{V}$ as the volume of the smallest curved environment through which a given robot can pass and Figure 17 illustrates this concept. We assume a rigid robot link is cylindrical with diameter w_r and length L_r. Figure 17(a) depicts a rigid link advancing through the link's minimum confining space, parameterized by the environment's radius r_e and its curvature κ_e. The minimum confining space is dependent on both the link's geometry and the environment's curvature. A segment of a continuum manipulator with the same initial cylindrical dimensions as the rigid link is advanced through the segment's minimum confining space given the same environmental curvature in Figure 17(b). Noticeably, the robot and environment radius only differ by ϵ to account for
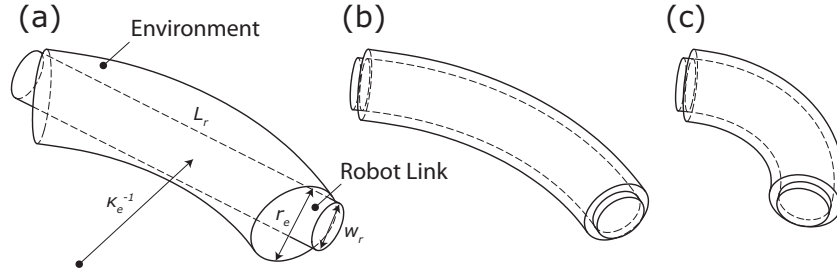
Fig. 17. (a) A rigid robot link advancing through its minimum confining space at a given environmental curvature κ_e. (b) A soft robot link advancing through its minimum confining space given the same environmental curvature. (c) A soft robot link advancing through its minimum confining space given an increased environmental curvature.
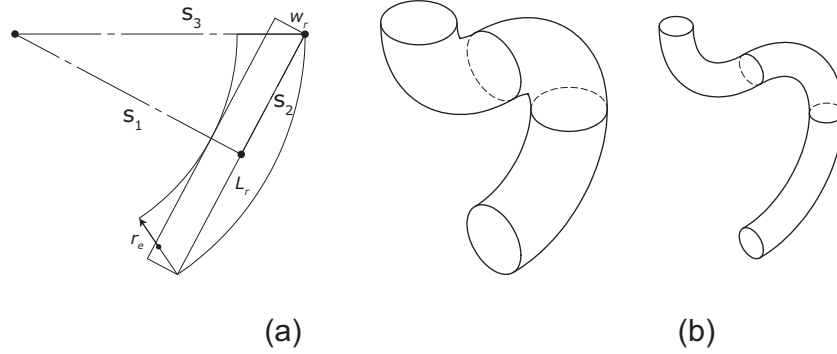
Fig. 18. (a) The triangle with sides s_1, s_2, and s_3 is constructed and used in determining the relationship between environmental radius r_e and environment curvature κ_e and robot link diameter w_r and length L_r. (b) A visualization of the volume difference between hard and soft minimum confining spaces for a robot link aspect ratio of six to one and an environment bend angle of $\pi/2$.

circumferential expansion under actuation. Lastly, in Figure 17(c) it is shown that the curvature of the environment is only limited by the curvature bounds of the continuum segment.

More concretely, we can write $\hat{V}$ as a function of robot link geometry, L_r and w_r. By using the geometric construction outlined in Figure 18(a) we can express $\hat{V}_H$, or the minimum confining space for a rigid link. We start by finding the environment radius r_e via the triangle composed of sides s_1, s_2, and s_3 and the law of cosines

$$s_1 = \frac{1}{\kappa_e} - r_e + w_r \tag{21}$$

$$s_2 = \frac{L_r}{2} \tag{22}$$

$$s_3 = \frac{1}{\kappa_e} + r_e \tag{23}$$

$$r_e = \frac{1}{8} \frac{8 w_r + 4 w_r^2 \kappa_e + L_r^2 \kappa_e}{2 + w_r \kappa_e} \tag{24}$$

$$\frac{\partial r_e}{\partial \kappa_e} = \frac{1}{4} \frac{L_r^2}{(2 + w_r \kappa_e)^2} \tag{25}$$

An important observation is that under these assumptions the environment radius always increases with curvature.

Next, the environment's bending angle θ_e can be found using the law of sines

$$\theta_e = 2 \, \mathbb{R}\left(\arcsin\left(\frac{1}{2} \frac{L_r \kappa_e}{1 + r_e \kappa_e} \right) \right) \tag{26}$$

and using the volume of a torus scaled by the bending angle we can express $\hat{V}_H$

$$\hat{V}_H(w_r, L_r, \kappa_e) = 2 \, \pi^2 \, \frac{1}{\kappa_e} \, r_e^2 \left(\frac{\theta_e}{2 \, \pi} \right) \tag{27}$$

For a continuum manipulator the expression for the minimum confining space $\hat{V}_S$ is similar but with the difference that r_e is not necessarily a function of κ_e. In fact, in the ideal case r_e is constant and equal to $w_r/2 + \epsilon$ where ϵ accounts for the circumferential strain and/or clearance. Then,

$$\hat{V}_S(w_r, L_r, \kappa_e) = 2 \, \pi^2 \, \frac{1}{\kappa_e} \left(\frac{w_r}{2} \right)^2 \left(\frac{\theta_e}{2 \, \pi} \right) \tag{28}$$

This implies the minimum confining space for a continuum manipulator segment can be significantly smaller than a rigid manipulator link in this class of environments. This illustrated in Figure 19 which shows the ratio $\hat{V}_H/\hat{V}_S$ as a function of κ_e at various manipulator link aspect ratios, $L_r : w_r$. Under the aforementioned assumptions, as $\epsilon \to 0$ a continuum robot will always be able to advance through a
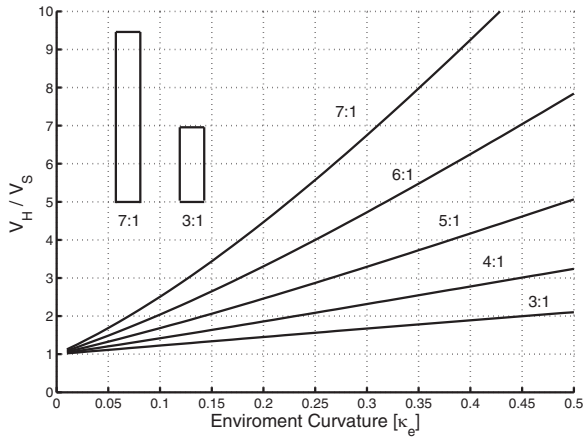
Fig. 19. The ratio of a hard to soft robot's minimum confining volume $\widehat{V_H}/\widehat{V_S}$ as a function of the curvature of the surrounding environment κ_e. The robot's minimum confining volume is the volume of the smallest curved environment through which a given robot can pass. The ratio is expressed for various robot link aspect ratios $L_r : w_r$. Both the hard and soft links have the same initial geometry.

smaller confining environment than a rigid linked robot when $\kappa_e > 0$. This volume difference increases with aspect ratio and environmental curvature. Figure 18(b) visualizes an example of this volume difference for a robot link aspect ratio of six to one and an environment bend angle of $\pi/2$.

6.1.1. Confined environment evaluations. For an entirely soft robot, where continuum kinematics and high compliance are combined, this result implies that such a manipulator can passively conform to the aforementioned class of confined environments. When the portion of the arm within the confined environment is passive $\epsilon \rightarrow 0$ and when the environment is composed of PCC cylinders, the above assumptions are met. In order to experimentally validate the soft fluidic elastomer manipulator's ability to advance through a confined environment we autonomously advance a passive manipulator with an actuated base through a pipe. Then, we actively perform a task once the manipulator is fully inserted. The experiment is shown in Figure 20 as well as Extension 1. The goal of the experiment is to repeatably advance the soft arm (Figure 20b) through a tightly bending pipe (Figure 20(d)) using only a constant linear and rotational motion of the manipulator's base. This insertion motion is provided by a motorized rotary and linear stage (Figure 20(h) and (i), respectively). A camera located at the arm's end effector (Figure 20(c)) can be used to localize the pipe entrance, inspect the pipe, and view objects of interest (Figure 20(f)) once the arm has exited the pipe. Video from this end effector camera is shown in the supplementary video submission. Because the arm's fluidic transmission system can deliver power independent of the arm's configuration, a tether (Figure 20(e)) allows the user to actuate the most distal segment while the proximal portion

of the arm has passively conformed to the pipe environment, as is shown in Extension 1.

10 consecutive trials of the confined environment experiment were performed, and the manipulator successfully advanced through the pipe in every trial and was able to perform an actuated task after insertion every trial. The confined environment consists of three 5 cm insider diameter bent pipe segments each with a curvature of approximately $15.2\,\mathrm{m}^{-1}$, motivated by the fact that the manipulator's maximum outside diameter is five centimeters with a two degree taper from tip to base. In all tests the manipulator's base was moved at a constant linear velocity and rotational velocity of 12 mm/s and 0.11 rev/s, respectively. The base was moved until a fixed insertion depth of 40 cm was reached. A thin layer of Talc powder was applied to the surface of the silicone arm to reduce the coefficient of friction between the robot's surface and plastic pipe. A load cell (Figure 20(g)) was used to measure insertion force as a function of time. Figure 21 shows this required resulting insertion force and insertion depth as a function of time for all ten trials as well as the applied base linear and rotational velocities as a function of time. Across the ten trials the mean peak insertion force was $11.8 \pm 1.2\,\mathrm{N}$.

It should be noted that we did not investigate pipe insertions where the gross motion of the robot is orthogonal or even opposite to gravity. We imagine that our current approach to passive insertion may not be well-suited for either of these scenarios. By employing a retractable sheath extending to the tip of the manipulator (as opposed to the static, base-segment sheath employed in the current experiments) it is conceivable that the uninserted portion of the manipulator could be sufficiently supported, potentially allowing for such insertion scenarios.
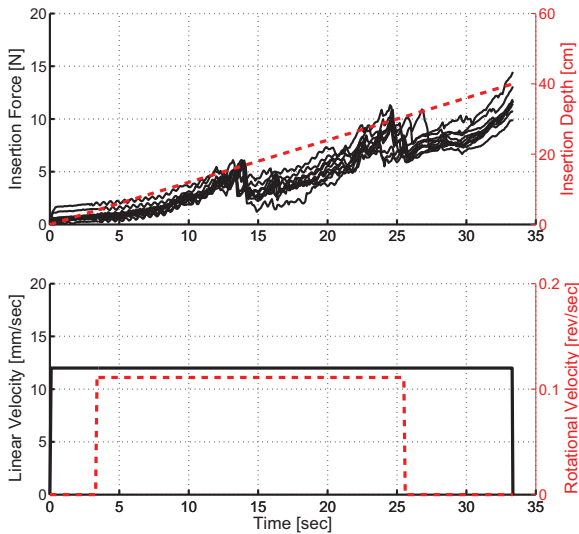
6.2. Shape fitting

The continuum kinematics of a soft robot manipulator enable a high degree of dexterity. Specifically, in an environment where a collision-free path is parameterized by a curved shape, a continuum manipulator can generally fit the curvature of the path better than a rigid link manipulator with discrete joints. Consider a path in planar cartesian coordinates $P(x(t), y(t))$ parameterized by time t or equivalently arc length s. The curvature at t can be expressed as

$$\kappa_p(t) = \left(\frac{\partial x}{\partial t}\frac{\partial^2 y}{\partial t^2} - \frac{\partial y}{\partial t}\frac{\partial^2 x}{\partial t^2}\right) \Big/ \left(\frac{\partial x^2}{\partial t} + \frac{\partial y^2}{\partial t}\right)^{3/2} \quad (29)$$

Because the first order Taylor series expansion $TS_1(\kappa_p(t))$ at t is constant, a soft continuum robot has the capacity to locally approximate the path's curvature to the first order by adjusting the curvature of its neutral axis over a continuum. In the case of no external forces, each of the soft continuum N segments can be fit to approximate the local curvature of the path under actuation
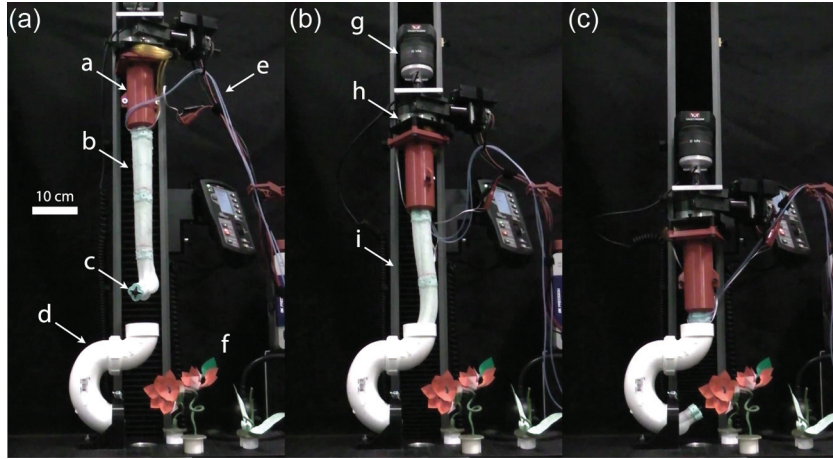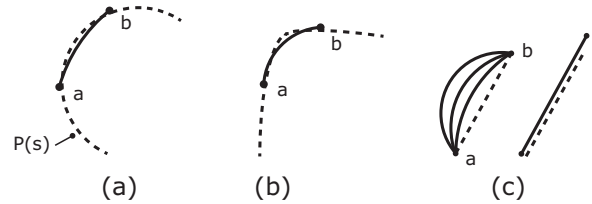
Fig. 20. Pipe insertion experiment. The experimental setup consists of serval components: (a) plastic sheath, (b) soft manipulator prototype of maximum outside diameter 5 cm, (c) end effector camera, (d) confining pipe of inside diameter 5 cm, (e) power tether, (f) objects of interest, (g) load cell, (h) automated rotary stage, and (i) automated linear stage. (A) Depiction of the manipulator prior to pipe insertion. Here, the distal most arm segment is actuated to simulate localization of the pipe entrance. (B) Depiction of the passive arm being autonomously inserted through the pipe by means of actuation at its base. (C) Depiction of the manipulator fully advanced through the pipe and performing the actuated task of inspecting flowers with its end effector camera.

Fig. 22. Several common scenarios that cause an error between a continuum robot's curvature and a path's curvature. (a) The maximum curvature of the robot is less than the local curvature of the path on the interval $s = [a,b]$. (b) The local curvature of the path is non-constant and the robot's deformation is parameterized by PCC arcs. (c) Description of a scenario where the robot's segment length is greater than the total path length.

Fig. 21. Results of pipe insertion experiment. At the top, measured insertion force as well as insertion depth is reported for all 10 experimental trials. Generally the insertion force increased with the insertion depth. At the bottom, the commanded linear and rotational velocity of the manipulator's base are shown during the insertion phase of the experiment. The insertion phase has positional end criteria, that is linear velocity is constant at 12 mm/s until a fixed insertion depth of 40 cm is reached upon which motion is stopped. Note that base rotation begins several seconds after linear motion, approximately when the manipulator enters the pipe, and base rotation has a fixed velocity of 0.11 rev/s until 2.43 revolutions are reached.

$$\kappa_i = \frac{1}{L_i} \int_{-\frac{L_i}{2}}^{\frac{L_i}{2}} TS_1\left(\kappa_p(s)\right) \mathrm{d}s \quad \forall\, i = 1, \dots, N \qquad (30)$$

where L is the soft segment length. There are several scenarios that cause an error between the continuum robot's curvature and the path's curvature. These scenarios are detailed in Figure 22. Figure 22(a) depicts a scenario where the path $P(s)$, shown by the dotted line, has locally constant curvature on the interval $s = [a, b]$; however, the arm segment's neutral axis of approximately equal length, shown as the solid line, has a maximum curvature $\kappa^{\max}$ less than $\kappa_p(s)$ and this produces an error in shape fitting. Figure 22(b) depicts a scenario where the path's local curvature on the interval $s = [a, b]$ is non-constant and this also causes an error in the goodness of fit between the path and arm segment of approximately equal length. Lastly, Figure 22(c) illustrates the scenario where the arm segment length L is greater than the total path length. Although a quality shape fit may be possible, this results in positional error either normal to the path (left) or tangent to the path (right).

Algorithm 3. Path fitting algorithm (for `forwardKin()` see Algorithm 4).

for $t = 0 : dt : t_f$ **do**

1     $s \leftarrow t \dfrac{\Delta s}{dt}$.

2     $N, \mathbf{L} \leftarrow$ Determine the number of segments N that can be projected onto P and their corresponding lengths $\mathbf{L}$ as a function of s and $\mathbf{L}_0$.

3     $\kappa^* \leftarrow \begin{cases} \underset{\kappa}{\min} & \sum\limits_{i=1}^{N} \left\| \mathrm{forwardKin}\!\left(\kappa, \mathbf{L}, i, L_i\right) - P\!\left(\sum\limits_{j=1}^{i} L_j\right) \right\| + \sum\limits_{i=1}^{N} \left\| \mathrm{forwardKin}\!\left(\kappa, \mathbf{L}, i, \frac{L_i}{2}\right) - P\!\left(\sum\limits_{j=1}^{i} L_j - \frac{L_i}{2}\right) \right\| \\ \text{subject to} & \kappa_i^{\min} \leq \kappa_i \leq \kappa_i^{\max} \quad \forall i = 1\,N. \end{cases}$

4   Servo continuum segments to $\boldsymbol{\kappa}^*$

end

In the case of a rigid link manipulator with discrete joints, curvature along the neutral axis is either $\pm\infty$, as by definition this structure is not a continuum. In this case the best way to approximate the curvature of a path is to increase the number of links and decrease the link length relative to the path length.

6.2.1. Shape fitting algorithm. To incrementally advance a soft continuum manipulator along a curved path we propose the path following strategy described in Algorithm 3. The fundamental idea of this path following approach is that each segment is sequentially advanced onto the path. For each segment on the path, two points along the segment's neutral axis, the mid and endpoint, are fit to the path by choosing the segment's curvature κ to minimize the Euclidean norm between the two points and their projection onto the path. By adding two points for each segment advanced onto the path plus the origin pose constraint, this approach effectively samples the path's curvature $\kappa_p(s)$ as two points and an initial orientation uniquely define a constant curvature arc. This approach assumes the manipulator has the capacity to position and orient a point along its neutral axis that is a distance s from the manipulator's tip, to the path's origin.

`forwardKin()` or the forward kinematics procedure (see Algorithm 4) for recursively determining a point on the arm located a distance s on segment i given curvature and length was developed in Marchese et al. (2014b).

6.2.2. Shape fitting simulations. To demonstrate the difference between fitting a soft continuum and rigid-linked robot to a curved path, we perform several simulations of advancing both a soft and rigid manipulator backbone through a curved path. The results of the simulations are shown in Figure 23. The first column describes a given collision free path through an environment. Columns two through four show the backbone of a soft robot (blue) and hard robot (red) advancing along and conforming to the path with different link lengths. Their neutral axis is overlaid at every time step. Both the soft and hard manipulators have the same link length, and this is varied from 25% of the total path length in column two to 41% of path length

---

Algorithm 4. Forward kinematics algorithm.

Procedure `forwardKin` ($\boldsymbol{\kappa}, \boldsymbol{L}, i, s$)

Input: $\boldsymbol{\kappa}, \boldsymbol{L}, i$ the segment of interest index, s the arc length along the indexed segment

if $i = 0$ **then**

    $\theta_i(0) \leftarrow \theta_0(0)$.

    $x_i(0) \leftarrow 0$.

    $y_i(0) \leftarrow 0$.

else

    $[x_i(0), y_i(0), \theta_i(0)] \leftarrow$ `forwardKin` ($\boldsymbol{\kappa}, \boldsymbol{L}, i-1, L_{i-1}$).

end

$\theta \leftarrow \theta_i(0) + k_i s$.

$x \leftarrow x_i(0) + \dfrac{\sin\theta}{k_i} - \dfrac{\sin\theta_i(0)}{k_i}$.

$y \leftarrow y_i(0) - \dfrac{\cos\theta}{k_i} + \dfrac{\cos\theta_i(0)}{k_i}$.

return $[x, y, \theta]^\mathrm{T} or [x, y]^\mathrm{T}$

---

in column four. In general, as the ratio of link length to path length increases the number of error scenarios outlined in Figure 22 increases, and the quality of fit decreases; However, in these examples the soft continuum robot approximated the curved path better than the rigid link robot in all cases.

6.2.3. Single segment tracking experiments. First, we seek to experimentally evaluate the ability of the closed-loop controller, developed in Section 5, to regulate the curvature of an individual arm segment. These experiments differ from those in Marchese et al. (2014b) in that they are performed using the spatial manipulator described in Section 3 which is an entirely new hardware system and with a hanging manipulator that is subject to gravitational loading and not supported by a plane. Figure 24 details a series of experiments where a sinusoidal reference curvature is tracked by the controller. The left-hand and right-hand columns represent reference waves with angular frequencies of 0.16 and 0.63 rads/sec, respectively.

Experiment 1 details the performance of the controller tracking a wave centered about zero curvature. Notably, the system has difficulty tracking curvatures around zero. A
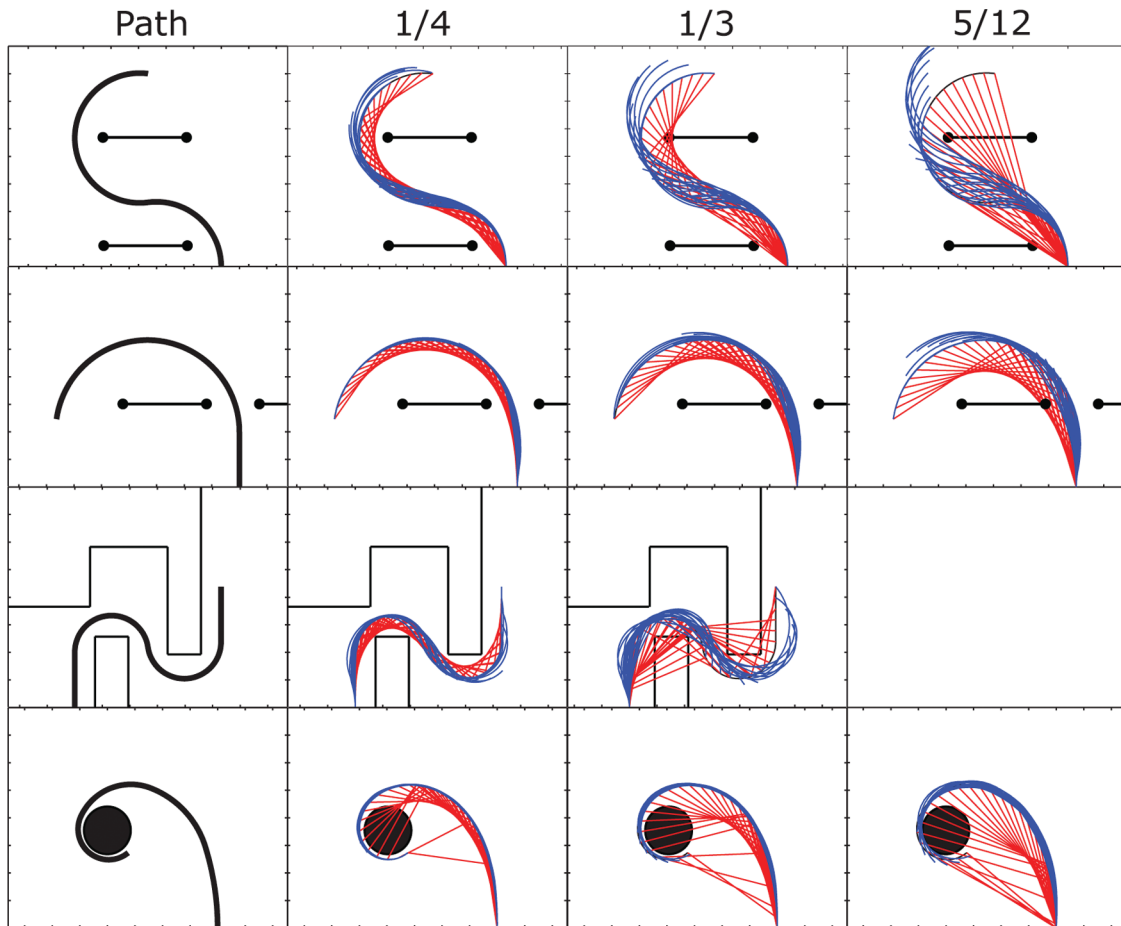
Fig. 23. Shape fitting simulations. In the first column, a collision free curved path through several environments is given. In the second, third, and fourth columns a soft robot with a PCC backbone (Webster and Jones, 2010), shown in blue, and a hard robot with fixed joints, shown in red, are sequentially advanced along and fit to the path in the first column using Algorithm 3. Manipulator link length is varied from 25% of total path length in column two to 41% of path length in column four as indicated by the ratios above each column.

likely explanation for this behavior is the severe nonlinear deformation encountered when inflating a thin-walled tube detailed in Gent (2012). In short, there can be two stable configurations of the expanding tube for a given internal pressure above a certain critical pressure. Evidence of this behavior can be observed directly in Figure 10(b). Although the actuated channel is uniformly pressurized, the elastomer exhibits both aneurysm-like areas of large deformation as well as areas of relatively small deformation. We attribute the difficulty in regulating segment curvature around zero to the nonlinear, bi-stable deformation characteristics of this particular channel geometry.

During Experiment 2, the same reference trajectories were tracked; however, the agonist and antagonist channels were each pre-filled with 50 ccm of air prior to the start of the experiment and automatic piston adjustments. Our hypothesis is that by pre-pressurizing the channels, the critical inflation pressure can be achieved with smaller piston motions and thus the large deformation configuration (the deformation responsible for producing appreciable

curvature) is reached with less delay. Experimentally, we observed improvements in tracking performance using this method; however, these improvements were not consistent throughout Experiment 2. For example, while tracking the lower frequency wave the actuated channel responsible for negative curvature performed almost identical between Experiment 1 and 2, despite the added pre-pressurization. Again, we attribute this to the fact that a large and small deformation configuration are both viable and stable at these inflation pressures. We observed performance improvements while tracking the higher frequency wave with the pre-pressurization approach.

Lastly, Experiment 3 shows the ability of the controller to track the low and high frequency curvature trajectories without pre-pressurization when the wave trajectory is biased away from zero. In this experiment, the offset of the sine wave begins at zero and is gradually increased to $7.5 \, \mathrm{m}^{-1}$ where it is held. As expected, initial tracking about near-zero curvatures is difficult, but once the bias sufficiently increases the tracking performance improves. The
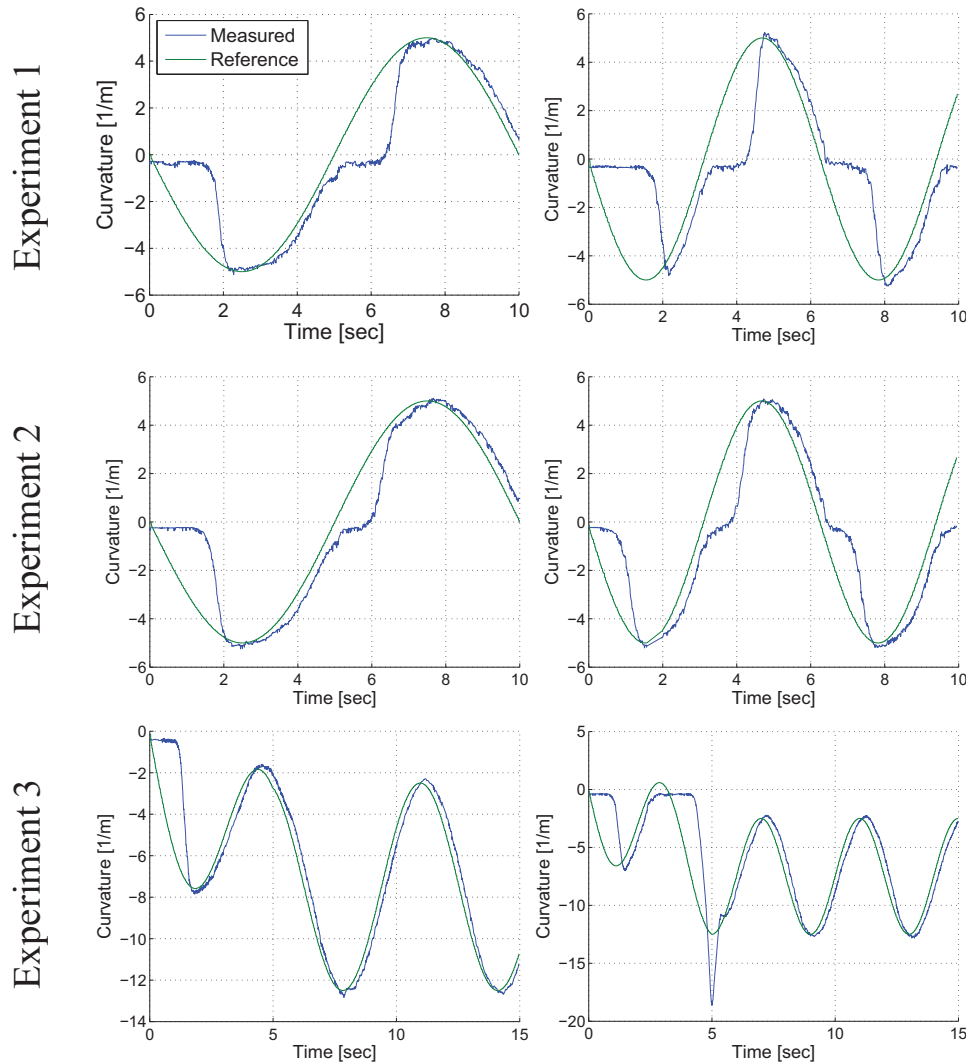
Fig. 24. A series of experiments characterizing the performance of the control system to track sine wave reference trajectories. In Experiment 1 the wave offset is zero, in Experiment 2 the wave offset is again zero but the channels are pre-pressurized, and lastly during Experiment 3 the offset is gradually increased away from zero to a fixed $7.5\,\mathrm{m}^{-1}$ and no pre-pressurization is used.

bias effectively serves to keep the inflation pressure above the pressures resulting in the bi-stable channel deformations.

6.2.4. Multi-segment tracking experiments. The purpose of the experiments performed in this section is to evaluate the aggregate soft manipulation system's ability to autonomously control the configuration of the soft arm. That is, in real-time with the closed-loop controller developed in Section 5, we drive the arm's measured curvature representation $\kappa_{\mathrm{measured}}$ to a desired reference shape parameterized by κ_{target}. We demonstrate that the arm is able to conform to a user specified configuration within a sagittal plane index by γ. To the best of our knowledge, this is the first demonstration of closed-loop curvature control for a fluidic elastomer robot not constrained to planar motion.

The goal of the experiments detailed in Figures 25 and 26 as well as in Extension 2 is for the soft manipulator to

autonomously transition from a neutral, hanging state (i.e. $\theta_0 = 3\pi/2$ and $\kappa_0 \approx \mathbf{0}$) to either an S shape (see Figure 25) or a C shape (see Figure 26). Ten and twelve trials of the S and C shape experiments were performed, respectively, and the results for all trials are shown in Figures 25 and 26, respectively. In the S-shaped configuration experiment, segments were less prone to twisting about their neutral axis (an unactuated DOF), and accordingly it was sufficient to use a single pair of agonist actuators collocated with the sagittal plane to achieve the required bending (schematically represented Figure 5C(d)). However, during the C-shaped configuration experiment, segments were more prone to twisting about their neutral axis. To counter this phenomenon, two pairs of agonist actuators were collocated with the sagittal plane, i.e. each pair was offset 45° from the sagittal plane (schematically represented Figure 5C(c)). This actuation strategy provides equal and opposite components of force that stabilize the segment's bending along the sagittal plane.
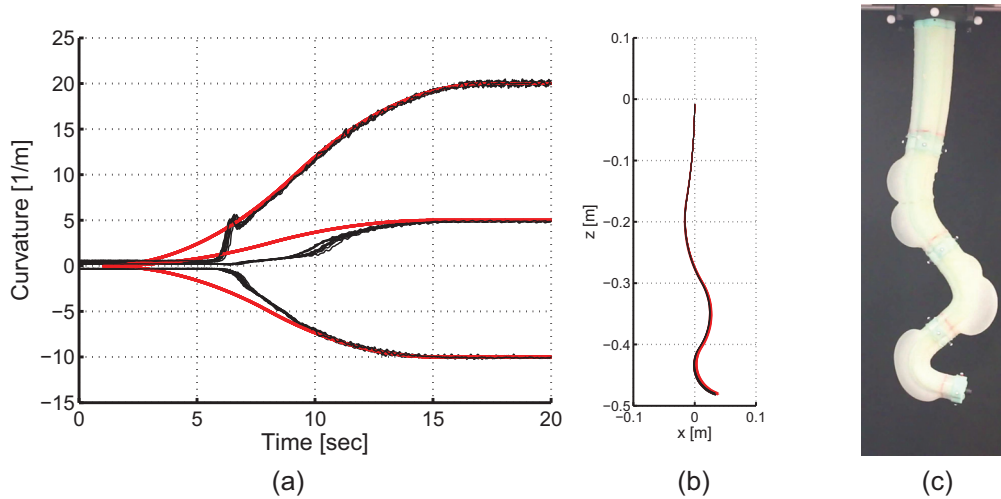
Fig. 25. Experimental evaluations of closed-loop real-time configuration control. In 10 consecutive trials, the aggregate manipulation system is provided an S shaped goal configuration to reach, shown in red in (b). The goal configuration state is parameterized by three target curvatures $\kappa_f=[5, -10, 20]$ for segments two to four respectively. Algorithm 2 plans a reference configuration trajectory $\kappa(t)$, shown in red in (a), and drives the arm along this configuration trajectory by measuring the arm's current configuration, shown in black in (a), and adjusting the volumetric displacement of the fluidic drive cylinder array. (c) The prototype fluidic elastomer manipulator in the target configuration.
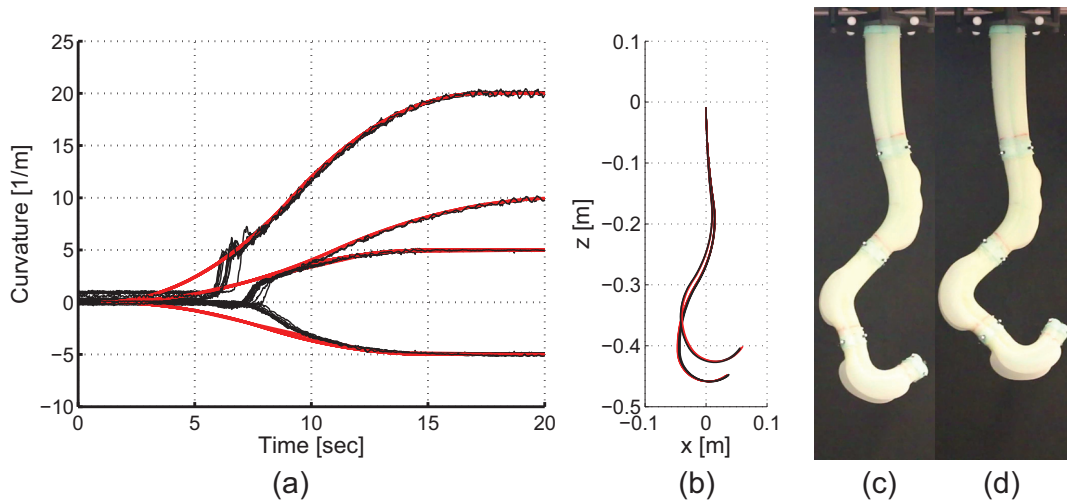
Fig. 26. Experimental evaluations of closed-loop real-time configuration control. In 10 consecutive trials, the aggregate manipulation system is provided a C shaped goal configuration to reach, shown in red in (b). The goal configuration state is parameterized by three target curvatures and 10 trials used the goal $\kappa_f=[-5, 5, 20]$ and two trials used the goal $\kappa_f=[-5, 10, 20]$ for segments two to four respectively. Algorithm 2 plans a reference configuration trajectory $\kappa(t)$, shown in red in (a), and drives the arm along this configuration trajectory by measuring the arm's current configuration, shown in black in (a), and adjusting the volumetric displacement of the fluidic drive cylinder array. (c, d) The prototype fluidic elastomer manipulator in the target configurations. (d) Reproduced with kind permission from Mary Ann Liebert Inc. (Marchese et al., 2015a)

Panel (a) in Figures 25 and 26 depicts the reference curvature trajectory, $\kappa_{\text{target}}(t)$, in red and measured curvature trajectory, κ_{measured}, in black as a function of time, as determined by Algorithm 2 developed in Section 5. Note that, three out of the four segments are actively controlled, and the base segment is left passive in order to dampen oscillations arising from distal segment movement. Panel (b) shows the reference (red) and measured (black) manipulator configuration at $t=20$. Panel (c) contains photographs of the soft fluidic elastomer arm prototype during the experiments. The mean one standard deviation steady state curvature errors across all the trials for the C shape were 0.05 ± 0.09, -0.04 ± 0.07, and $0.02 \pm 0.09\,\text{m}^{-1}$, respectively for segments two through four respectively. The steady state curvature errors across all the trials for the S shape were -0.11 ± 0.03, -0.02 ± 0.07, and $0.03 \pm 0.12\,\text{m}^{-1}$, respectively.

Algorithm 5. Algorithm for three-dimensional positioning.

Procedure `moveToObject()`

  $[x_{\text{object}}, y_{\text{object}}, z_{\text{object}}] \leftarrow$ `localizeObject()`.

  $[x_{\text{offset}}, y_{\text{offset}}, z_{\text{offset}}]^{\mathrm{T}} \leftarrow \mathbf{T}_{\text{offset}}^{\text{object}} [x_{\text{object}}, y_{\text{object}}, z_{\text{object}}]^{\mathrm{T}}.$ `moveToPoint` $(x_{\text{object}}, y_{\text{object}}, z_{\text{object}})$.

return

Procedure `moveToPoint`$(x^{base}, y^{base}, z^{base})$

  $\gamma \leftarrow \arctan\left(\frac{y^{\text{base}}}{x^{\text{base}}}\right).$

  $[x^{\gamma}, y^{\gamma}, z^{\gamma}]^{\mathrm{T}} \leftarrow [\mathbf{T}_{\gamma}^{\text{base}}(\gamma)]^{-1} [x^{\text{base}}, y^{\text{base}}, z^{\text{base}}]^{\mathrm{T}}.$

  Move rotary stage to γ.

  while $\left| \text{forwardKin}(\kappa_{\text{meas}}, \mathbf{L}_{\text{meas}}, N, L_{\text{meas}_N}) - \begin{bmatrix} x^{\gamma} \\ z^{\gamma} \end{bmatrix} \right| \geq \epsilon$ **do**

    Wait until a new sensor measurement $\mathbf{E}^{\text{base}}$ is available.

    $\mathbf{E}_n^{\gamma} \leftarrow [\mathbf{T}_{\gamma}^{\text{base}}(\gamma)]^{-1} \mathbf{E}_n^{\text{base}} \quad \forall n = 1 \ldots N$

    $\boldsymbol{\kappa}_{\text{meas}}, \mathbf{L}_{\text{meas}} \leftarrow$ `singleSegInvKin`$(\mathbf{E}^{\gamma})$ (Marchese et al., 2014b)

    $\kappa_f \leftarrow \text{inverseKin}(x^{\gamma}, z^{\gamma}, \kappa_{\text{meas}_1})$

    $\dot{\boldsymbol{\kappa}}(t) \leftarrow \text{generateTraj}(\kappa_{\text{meas}}, \kappa_f, \dot{\boldsymbol{\kappa}}^{\text{max}}, \ddot{\boldsymbol{\kappa}}^{\text{max}})$

    $\text{driveSegments}(\dot{\boldsymbol{\kappa}}(t), \gamma);$

  end

return

Procedure `inverseKin`$(x, y, \kappa_{\text{meas}_1})$

  $\mathbf{R}$ a weighting vector,

  θ^{min} and θ^{max} constraints on end-effector approach angle.

  $\kappa^* \leftarrow \min_{\kappa} \quad \sum_{i=1}^{N} R_i \kappa_i$

  subject to $\quad \mathbf{f} \leftarrow \text{forwardKin}(\kappa, \mathbf{L}_{\text{meas}}, N, L_{\text{meas}_N})$

  $\qquad\qquad\qquad \begin{bmatrix} x \\ y \end{bmatrix} - \begin{bmatrix} f_1 \\ f_2 \end{bmatrix} = \mathbf{0}$

  $\qquad\qquad\qquad \kappa_{\text{meas}_1} - \kappa_1 = 0$

  $\qquad\qquad\qquad \theta^{\text{min}} \leq f_3 \leq \theta^{\text{max}}$

  return $\boldsymbol{\kappa}^*$ $\qquad \kappa_n^{\text{min}} \leq \kappa_n \leq \kappa_n^{\text{max}} \quad \forall n = 1, \ldots, N$
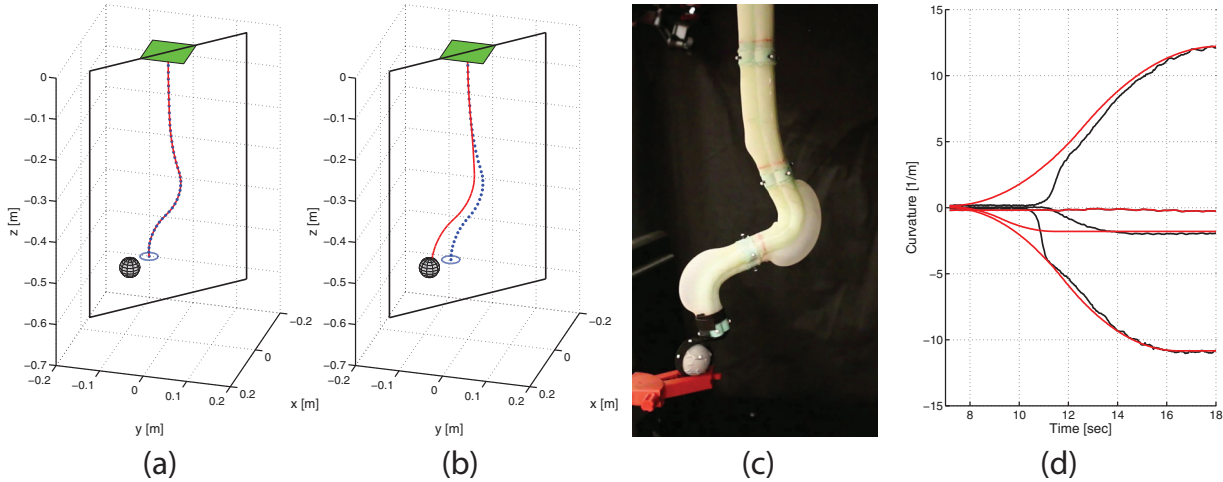

6.3. Positioning

Additionally the soft arm is capable of Cartesian positioning in three dimensions. Similar to the approach in Marchese et al. (2014a), we pose the inverse kinematics problem (i.e., the transformation from the manipulator's task space to its arc space) as a constrained nonlinear optimization, allowing phenomena arising from the arm's softness to be expressed as numerical constraints. More specifically, we can calculate γ as well as find a locally-optimal reference configuration $\boldsymbol{\kappa}^*$ that position the arm's end-effector at a goal point within a statically reachable envelope. For more information on finding points within a statically reachable envelope please refer to Marchese et al. (2015b). Once a suitable reference configuration is determined, we can again use the procedures outline in Algorithm 2 to both plan an execute a curvature trajectory trajectory $\dot{\boldsymbol{\kappa}}(t)$.

6.3.1. Positioning algorithm. First, the procedure `moveToObject` in Algorithm 5 localizes an object's center in $\mathbb{R}^3$ using the external camera system, a process represented by `localizeObject()`. To obtain a target end-effector position, the object's position is translated a predetermined offset based on the object's geometry using the transformation $\mathbf{T}_{\text{offset}}^{\text{object}}$.

The strategy for moving the arm to this goal point is represented in the procedure `moveToPoint()`. First, the arm is rotated into a sagittal plane defined by the angle γ by means of the base rotary stage. The vertical plane is coincident with both the base frame's origin and the goal point. The end-effector is then iteratively moved in this plane towards the goal point by finding locally-optimal reference configurations. This iterative search for manipulator configurations starts, as previously mentioned, by taking a set of real-time endpoint measurements $\mathbf{E}_n^{\text{base}}$, projecting them into the sagittal plane using the simple transformation

Fig. 27. Experimental evaluations of three-dimensional end-effector positioning with the soft manipulator prototype. (a) Algorithm 5 plans a locally-optimal, minimal-strain reference configuration (red) to which the arm's measured configuration representation is driven (blue). Here, contact is made between the end-effector and object. (b) The algorithm's next plan is shown that would theoretically bring the manipulator's end-effector even closer to the intended target but physical contact with the object prevents the new target configuration from being reached. (c) A photograph of the manipulator's end effector making contact with the object of interest. (d) The first intermediate reference configuration trajectory $\kappa_{\text{target}}(t)$ is shown in red and the measured configuration representation of the manipulator is shown in black $\kappa_{\text{meas}}(t)$.

$\mathbf{T}_\gamma^{\text{base}}(\gamma)$ to arrive at the set $\mathbf{E}_n^\gamma$. This data is passed to the procedure `singleSegInvKin()` in order to uniquely fit a PCC model to the data, providing a measured manipulator configuration representation κ_{meas}. This provides the current manipulator configuration from which the trajectory $\dot{\kappa}(t)$ is started. To determine the trajectory's end configuration κ_f, the optimization-base inverse kinematics procedure, represented by `inverseKin()`, is invoked. This process finds a weighted minimal-strain solution subject to:

(a) the end-effector being positioned at the goal point projected into the sagittal plane;
(b) the state of the passive base segment, κ_{meas_1}, appropriately limiting the configuration's DOF;
(c) end-effector orientation being constrained, in combination with curvature limitations, in order to prevent configurations where the center of mass of segment n is above connector piece $n-1$ for static stability purposes; and
(d) empirically determined curvature limits not being exceeded.

After defining κ_{meas} and κ_f the previously defined procedure `generateTraj()` is used to generate a realizable configuration trajectory and the procedure `driveSegments()` is used to move the manipulator along this trajectory. The process is repeated until the end-effector is within ϵ of the goal location.

6.3.2. Positioning evaluations. In order to experimentally evaluate the three-dimensional positioning capabilities of

the soft arm we ran Algorithm 5 on the manipulation system. The goal of the experiment was for the soft arm to move its end-effector into contact with a 4 cm diameter table tennis ball placed within the arm's statically reachable envelope. The purpose of the experiment was to evaluate the arm's positioning capabilities, not to robustly pick-up the ball. Accordingly, velcro was simply fixed to both the ball and end-effector to perform the pick-up.

In 10 consecutive attempts, the manipulation system was able to successfully position the arm's end effector to make contact with the ball. The object offset translation $\mathbf{T}_{\text{offset}}^{\text{object}}$ underwent minor adjustments throughout the tests to continually improve the contact between the velcro pieces. Figure 27(a)–(d) as well as Extension 3 detail one of these trials. Figure 27(a) shows the first reference configuration κ_f planned by Algorithm 5 in red as well as the configuration representation κ_{meas} fit to measured endpoint data at $\mathbf{t}_f$ in blue. The discrepancy between κ_f and κ_{meas} is almost imperceptible. At this point the end-effector and object made contact (see 27(c)). Figure 27(b) shows the second reference configuration planned by the algorithm, considering the passive bending of the first segment, again shown in red. Noticeably, the manipulator's measured configuration representation, again shown in blue, deviates significantly from this plan as the manipulator's end-effector is already in contact with the object inhibiting the manipulator's motion in the desired direction. Lastly, Figure 27(d) shows intermediate target curvatures κ_{target} (red) as well as intermediate measured configuration representations κ_{meas} (black) from t_0 to t_f for each segment. The compressibility of the transmission medium as well as the relatively large residual volume of the pistons explain the several second

delay in tracking the reference configuration. We have recently shown that by using techniques such a prepressurization and tandem inflation this performance characteristic can be improved (Katzschmann et al., 2015).

7. Conclusion

In this work we presented an autonomous fluidic elastomer spatial manipulation system. We developed a new spatial manipulator morphology that is modular in design and well suited for automation. We constructed multiple physical prototypes of this soft arm using an innovative multi-step casting process that extends our approach to building manipulators from two dimensions (Marchese et al., 2014a) to three dimensions. We developed, simulateed, and experimentally validated a static model in order to understand how a single segment of this manipulator deforms. Then, using a piece-wise constant curvature assumption (Webster and Jones, 2010), we modeled the multi-segment kinematics of the soft manipulator. To power the manipulator, we developed an array of high capacity fluidic drive cylinders, again extending our approach to powering planar manipulation (Marchese et al., 2014b) into three dimensions. To control the arm in a rotating sagittal plane we developed a real-time closed-loop control algorithm that generates realizable curvature trajectories, measures the arms current state using localized segment endpoints, and leverages a cascaded control strategy we developed for our planar systems. These innovations in actuation, modeling, fabrication, power, and processing and control enable new manipulation capabilities for soft robots. We demonstrate the arm's ability to enter and advance through a confined spatial environment. We demonstrate that the soft manipulator prototype can use its passive compliance and softness to repeatedly advance through and conform to a complex pipe shape. In addition, because of its configuration-independent fluidic power transmission, the manipulator can perform actuated tasks with its distal most segments, once they have advanced through the confining environment. Another new capability is the aggregate soft manipulation system's ability to autonomously control the configuration of the soft arm. That is, in real-time with a closed-loop controller we show that a user-specified goal configuration can be repeatedly achieved with minimal shape error.

7.1. Limitations

There are several notable limitations within the presented work. In general, the presented actuator design does not explicitly consider the rupturing or failure of the elastic material. Although we have found the chosen physical dimensions of the soft elastomer actuators suitable for the number and type of experiments presented here, these are certainly not optimal and we also do not provide an investigation into the onset of plastic deformation or dynamic material fatigue. This is certainly a concern when actuator motions are fast, repetitive, and of relatively large magnitude. Furthermore, due to the nonlinear deformation profile of the presented channel geometry, the onset of these adverse phenomena may not be easy to predict.

Future work is needed to investigate the dynamic behavior of such elastomer-based robots. This study is limited to purely kinematic modeling and motion control. We have found this approach viable for controlling the configuration of the robot within a limited, statically reachable envelop; however, it is important to note that this reachable envelope is significantly constrained due to the force-limits of the proposed actuators and the need to compensate for the weight of multiple, distally suspended segments.

In addition, the developed soft manipulator has many passive DOFs and these can contribute to various motions both desirable and undesirable. For example, using the manipulator's passive DOFs we are able to achieve pipe insertion as detailed in Section 6.1; however, during configuration tracking experiments, passive DOFs lead to significant oscillations in the system's motion in the presence of external disturbances (please refer to Extension 1). In future work, a proper characterization of these passive DOFs could lead to model-based controllers that are capable of removing or even leveraging these phenomena.

References

Buckingham R (2002) Snake arm robots. _Industrial Robot: An International Journal_ 29(3): 242–245.

Calisti M, Arienti A, Giannaccini ME, et al. (2010) Study and fabrication of bioinspired octopus arm mockups tested on a multipurpose platform. In: _2010 3rd IEEE RAS and EMBS international conference on biomedical robotics and biomechatronics (BioRob)_, Tokyo, Japan, 26–29 September 2010, pp. 461–466. Piscataway: IEEE.

Calisti M, Giorelli M, Levy G, et al. (2011) An octopus-bioinspired solution to movement and manipulation for soft robots. _Bioinspiration and Biomimetics_ 6(3): 036002.

Camarillo DB, Carlson CR and Salisbury JK (2009) Configuration tracking for continuum manipulators with coupled tendon drive. *IEEE Transactions on Robotics* 25(4): 798–808.

Chen G, Pham MT and Redarce T (2006) Development and kinematic analysis of a silicone-rubber bending tip for colonoscopy. In: *2006 IEEE/RSJ international conference on intelligent robots and systems*, Beijing, 9–15 October 2006, pp. 168–173. Piscataway: IEEE.

Chirikjian GS and Burdick JW (1994) A hyper-redundant manipulator. *IEEE Robotics and Automation Magazine* 1(4): 22–29.

Cieslak R and Morecki A (1999) Elephant trunk type elastic manipulator-a tool for bulk and liquid materials transportation. *Robotica* 17(1): 11–16.

Correll N, Önal CD, Liang H, et al. (2014) Soft autonomous materials - using active elasticity and embedded distributed computation. In: Khatib O, Kumar V and Sukhatme G (eds) *Experimental Robotics: The 12th International Symposium on Experimental Robotics*. Berlin: Springer, 227–240.

Deimel R and Brock O (2013) A compliant hand based on a novel pneumatic actuator. In: *2013 IEEE international conference on robotics and automation*, Karlsruhe, Germany, 6–10 May 2013, pp. 2047–2053. Piscataway: IEEE.

Deimel R and Brock O (2014) A novel type of compliant, underactuated robotic hand for dexterous grasping. In: *Proceedings of robotics: science and systems*, 1687–1692. Available at: http://www.roboticsproceedings.org/rss10/p18.html (accessed 14 August 2015).

Gent AN (2012) *Engineering with Rubber: How to Design Rubber Components*. Munich: Carl Hanser Verlag GmbH Co. KG.

Giorelli M, Renda F, Calisti M, et al. (2012) A two-dimensional inverse kinetics model of a cable driven manipulator inspired by the octopus arm. In: *2012 IEEE International conference on robotics and automation*, Saint Paul, USA, 14–18 May 2012, pp. 3819–3824. Piscataway: IEEE.

Gravagne IA, Rahn CD and Walker ID (2003) Large deflection dynamics and control for planar continuum robots. *IEEE/ASME Transactions on Mechatronics* 8(2): 299–307.

Gravagne IA and Walker ID (2002) Uniform regulation of a multisection continuum manipulator. In: *Proccedings of the ICRA 2002 IEEE international conference on robotics and automation, vol. 2*, Washington, DC, USA, 11–15 May 2002, pp. 1519–1524. Piscataway: IEEE.

Hannan MW and Walker ID (2003) Kinematics and the implementation of an elephant's trunk manipulator and other continuum style robots. *Journal of Robotic Systems* 20(2): 45–63.

Jones BA and Walker ID (2006a) Kinematics for multisection continuum robots. *IEEE Transactions on Robotics* 22(1): 43–55.

Jones BA and Walker ID (2006b) Practical kinematics for realtime implementation of continuum robots. *IEEE Transactions on Robotics* 22(6): 1087–1099.

Kang R, Branson DT, Zheng T, et al. (2013) Design, modeling and control of a pneumatically actuated manipulator inspired by biological continuum structures. *Bioinspiration and Biomimetics* 8(3): 036008.

Katzschmann RK, Marchese AD and Rus D (2014) Hydraulic autonomous soft robotic fish for 3d swimming. In: *International symposium on experimental robotics (ISER)*, Marrakech and Essaouira, Morocco, 15–18 June 2014 (in press).

Katzschmann RK, Marchese AD and Rus D (2015) Autonomous object manipulation using a soft planar grasping manipulator (in press).

Laschi C, Cianchetti M, Mazzolai B, et al. (2012) Soft robot arm inspired by the octopus. *Advanced Robotics* 26(7): 709–727.

McEvoy MA and Correll N (2014) Shape change through programmable stiffness. In: *International symposium on experimental robotics*, Marrakech and Essaouira, Morocco, 15–18 June 2014 (in press).

McMahan W, Chitrakaran V, Csencsits M, et al. (2006) Field trials and testing of the octarm continuum manipulator. In: *Proceedings 2006 of the IEEE international conference on robotics and automation*, Orlando, USA, 15–19 May 2006, pp. 2336–2341. Piscataway: IEEE.

McMahan W, Jones BA and Walker ID (2005) Design and implementation of a multi-section continuum robot: Air-octor. In: *2005 IEEE/RSJ international conference on intelligent robots and systems*, Edmonton, Canada, 2–6 August 2005, pp. 2578–2585. Piscataway: IEEE.

Mahl T, Mayer AE, Hildebrandt A, et al. (2013) A variable curvature modeling approach for kinematic control of continuum manipulators. In: *2013 american control conference*, Washington, DC, USA, 17–19 June 2013, pp. 4945–4950. Piscataway: IEEE.

Marchese AD, Katzschmann RK and Rus D (2014a) Whole arm planning for a soft and highly compliant 2D robotic manipulator. In: *2014 IEEE/RSJ international conference on intelligent robots and systems*, Chicago, USA, 14–18 September 2014, pp. 554–560. Piscataway: IEEE.

Marchese AD, Komorowski K, Onal CD, et al. (2014b) Design and control of a soft and continuously deformable 2D robotic manipulation system. In: *2014 IEEE international conference on robotics and automation*, Hong Kong, China, 31 May–7 June 2014, pp. 2189–2196. Piscataway: IEEE.

Marchese AD, Katzschmann RK and Rus D (2015a) A recipe for soft fluidic elastomer robots. *Soft Robotics* 2(1): 7–25.

Marchese AD, Onal CD and Rus D (2011) Soft robot actuators using energy-efficient valves controlled by electropermanent magnets. In: *2011 IEEE/RSJ international conference on intelligent robots and systems*, San Francisco, USA, 25–30 September 2011, pp. 756–761. Piscataway: IEEE.

Marchese AD, Onal CD and Rus D (2014c) Autonomous soft robotic fish capable of escape maneuvers using fluidic elastomer actuators. *Soft Robotics* 1(1): 75–87.

Marchese AD, Tedrake R and Rus D (2015b) Dynamics and trajectory optimization for a soft spatial fluidic elastomer manipulator. In: *2015 IEEE international conference on robotics and automation (ICRA)*, Seattle, USA, 26–30 May 2015, pp. 2528–2535. Piscataway: IEEE.

Martinez RV, Branch JL, Fish CR, et al. (2013) Robotic tentacles with three-dimensional mobility based on flexible elastomers. *Advanced Materials* 25(2): 205–212.

Miura K and Furuya H (1988) Adaptive structure concept for future space applications. *AIAA journal* 26(8): 995–1002.

Miura K, Furuya H and Suzuki K (1985) Variable geometry truss and its application to deployable truss and space crane arm. *Acta Astronautica* 12(7): 599–607.

Onal CD and Rus D (2013) Autonomous undulatory serpentine locomotion utilizing body dynamics of a fluidic soft robot. *Bioinspiration and Biomimetics* 8(2): 026003.

Onal CD, Chen X, Whitesides GM, et al. (2011) Soft mobile robots with on-board chemical pressure generation. In: *International symposium on robotics research*, Flagstaff, USA, 28 August–1 September 2011. Available at: http://www.isrr-2011.org/ISRR-2011/Program_files/Papers/Onal-ISRR-2011.pdf (accessed 14 August 2015).

Pritts MB and Rahn CD (2004) Design of an artificial muscle continuum robot. In: *Proceedings of the ICRA 2004 IEEE international conference on robotics and automation*, *vol. 5*, New Orleans, USA, 26 April–1 May 2004, pp. 4742–4746. Piscataway: IEEE.

Robinson G and Davies JBC (1999) Continuum robots-a state of the art. In: *Proceedings of the 1999 IEEE international conference on robotics and automation*, *vol. 4*, Detroit, USA, 10–15 May 1999, pp. 2849–2854. Piscataway: IEEE.

Sanan S, Moidel J and Atkeson C (2011) A continuum approach to safe robots for physical human interaction. In: *International symposium on quality of life technology (isQoLT)*, Toronto, Canada, 6–7 June 2011.

Shepherd RF, Ilievski F, Choi W, et al. (2011) Multigait soft robot. *Proceedings of the National Academy of Sciences* 108(51): 20400–20403.

Shepherd RF, Stokes AA, Freake J, et al. (2013) Using explosions to power a soft robot. *Angewandte Chemie* 125(10): 2964–2968.

Suzumori K, Iikura S and Tanaka H (1991) Development of flexible microactuator and its applications to robotic mechanisms. In: *Proceedings of the IEEE international conference on robotics and automation*, Sacramento, USA, 9–11 April 1991, pp. 1622–1627. Piscataway: IEEE.

Tolley MT, Shepherd RF, Mosadegh B, et al. (2014) A resilient, untethered soft robot. *Soft Robotics* 1(3): 213–223.

Trimmer BA, Takesian AE, Sweet BM, et al. (2006) Caterpillar locomotion: A new model for soft-bodied climbing and burrowing robots. In: *7th international symposium on technology and the mine problem vol. 1* Monteray, USA, 2–4 May 2006, pp. 1–10. Monterey: Mine Warfare Association.

Trivedi D, Rahn CD, Kier WM, et al. (2008) Soft robotics: Biological inspiration, state of the art, and future research. *Applied Bionics and Biomechanics* 5(3): 99–117.

Umedachi T, Vikas V and Trimmer B (2013) Highly deformable 3D printed soft robot generating inching and crawling locomotions with variable friction legs. In: *2013 IEEE/RSJ international conference on intelligent robots and systems (IROS)*, Tokyo, Japan, 3–7 November, pp. 4590–4595. Piscataway: IEEE.

Wang H, Chen W, Yu X, et al. (2013) Visual servo control of cable-driven soft robotic manipulator. In: *2013 IEEE/RSJ international conference on intelligent robots and systems (IROS)*, Tokyo, Japan, 3–7 November 2013, pp. 57–62. Piscataway: IEEE.

Webster RJ and Jones BA (2010) Design and kinematic modeling of constant curvature continuum robots: A review. *The International Journal of Robotics Research* 29(13): 1661–1683.

Webster RJ, Romano JM and Cowan NJ (2009) Mechanics of precurved-tube continuum robots. *IEEE Transactions on Robotics* 25(1): 67–78.

Appendix A: Index to Multimedia Extensions

Archives of IJRR multimedia extensions published prior to 2014 can be found at http://www.ijrr.org, after 2014 all videos are available on the IJRR YouTube channel at http://www.youtube.com/user/ijrrmultimedia

Table of Multimedia Extensions

Extension	Media type	Description
1	Video	A video of an exemplary experimental evaluation from Section 6.1. This video demonstrates the soft fluidic elastomer manipulator's ability to advance through a tightly bending pipe using only the constant linear and rotational motion of the manipulator's base.
2	Video	A video of exemplary experimental evaluations from Section 6.2. Here, the soft manipulator autonomously transitions from a neutral, hanging state (i.e. $\theta_0 = 3\pi/2$ and $\boldsymbol{\kappa}_0 \approx \mathbf{0}$) to either an S shape (see Figure 25) or a C shape (see Figure 26) under closed-loop configuration control.
3	Video	A video of exemplary experimental evaluations from Section 6.3. This video shows an experiment where the soft arm moves its end-effector into contact with a 4 cm diameter table tennis ball placed within the arm's statically reachable envelope.

Appendix B: Notation

$\mathbf{R}_x, \mathbf{R}_y, \mathbf{R}_z$	Rotation matrices about the subscript Cartesian axis in $\mathbb{R}^3$
$\mathbf{T}_x, \mathbf{T}_y, \mathbf{T}_z$	Translation matrices along the subscript Cartesian axis in $\mathbb{R}^3$
$\mathbf{T}$	Transformation matrix in $\mathbb{R}^3$
$\hat{\mathbf{i}}, \hat{\mathbf{j}}, \hat{\mathbf{k}}$	Unit vectors codirectional with the Cartesian coordinate system
κ, θ, L	Curvature, bend angle, and undeformed length of a soft arm segment's actuated region, respectively
$\boldsymbol{\kappa}_0, \boldsymbol{\kappa}_f,$ $\boldsymbol{\kappa}_{\text{meas}}, \boldsymbol{\kappa}_{\text{target}}$	Initial, final, measured representation, and target manipulator configuration vectors, respectfully
$\boldsymbol{\kappa}(t), \dot{\boldsymbol{\kappa}}(t),$ $\ddot{\boldsymbol{\kappa}}(t),$	Curvature, velocity, and acceleration configuration trajectories, respectfully
N	Total number of segments in a multi-segment manipulator
$\mathbf{E}_n^{\text{base}}, \mathbf{E}_n^{\gamma}$	A set of measured segment endpoint data in the base frame (i.e. $\subset \mathbb{R}^3$) and projected into the sagittal plane defined by γ (i.e. $\subset \mathbb{R}^2$), respectfully. The segment number is indexed by $n = 1, \dots, N$
θ_P, L_P	Bend angle and undeformed length of a soft arm segment's unactuated region, respectively
γ	Orientation of bend angle θ
s	Arc length

p_c	Channel fluid pressure	$\hat{V}$	Minimum confining spaces, or the smallest curved environment through which a given robot link can pass
σ_c, ϵ_c	Circumferential material stress and strain, respectively		
σ_L, ϵ_L	Longitudinal material stress and strain, respectively	$\hat{V}_H, \hat{V}_S$	Minimum confining space for a hard and entirely soft link, respectively
$\bar{h}, \bar{w}, \bar{t}, \bar{\theta}$	Channel diameter, wall length, wall thickness, and bend angle of a thin cross-sectional slice of a soft actuator, respectively	$w_r, L_r,$	Diameter and length of a cylindrical robot link
		r_e, κ_e, θ_e	Environment radius, curvature, and bend angle, respectively
$\hat{h}, \hat{w}, \hat{t}$	Deformed channel dimensions	P	A path in planar cartesian coordinates
$\bar{A}$	Cross-section area of a slice	κ_p	Path curvature
J	Total number of x–y cross-sectional slices of a segment's actuated region	TS_1	First order Taylor series expansion
		t	Time
θ^P, θ^M	Model predicted bending angle and measured bending angle, respectively	t_f	Final time
		$\mathrm{d}t$	Discrete time interval
G^P, G^M	Model predicted center of gravity and measured center of gravity. respectively		